INVESTIGATIONS ON NANOSCALE WETTING, FLUID TRANSPORT, AND DROPLET EVAPORATION AT NANOSTRUCTURED SURFACES BY MOLECULAR DYNAMICS SIMULATIONS

A Thesis Submitted to
the Graduate School of Engineering and Science of
İzmir Institute of Technology
in Partial Fulfillment of the Requirements for the Degree of

MASTER OF SCIENCE

in Energy Engineering

by
Ezgi ŞATIROĞLU

July 2021
İZMİR

ACKNOWLEDGMENTS

I would like to express my gratitude to my advisor, Assoc. Prof. Murat BARIŞIK for his endless support, patience, inspiring guidance, and continuous motivation during my days in Micro/Nano Engineering (MiNaEng) Group. I am always grateful to him for the courtesy of sharing his perspective, academic knowledge, and experience with me during my research and thesis.

I would like to thank The Scientific and Technological Research Council of Turkey (TUBITAK), for giving me the opportunity to carry out this research. This work is supported by TUBITAK under the grant number TÜBİTAK 217M460. I would also like to express my gratitude towards the Center for Scientific Computation at Southern Methodist University for enabling us to use their high-performance computing. I would like to thank to Turkish National e-Science e-Infrastructure (TRUBA) for providing me the computing infrastructure to perform this study.

It has been a pleasure to be a part of the MiNaEng Research Group. I would like to express my deepest gratitude to my colleagues in the research group.

I would like to express my greatest appreciations to my family, my mother Hülya ŞATIROĞLU and my father Ercüment ŞATIROĞLU for their endless support, encouragement and love throughout my entire life and education. I also would like to express my sincere thanks to İsmail Gürkan DEMİRKIRAN for his valuable support, endless help and motivation during my study. He has always believed in me and encouraged me to reach further.

ABSTRACT

INVESTIGATIONS ON NANOSCALE WETTING, FLUID TRANSPORT, AND DROPLET EVAPORATION AT NANOSTRUCTURED SURFACES BY MOLECULAR DYNAMICS SIMULATIONS

There is a significant need to understand solid-liquid interactions at nanoscale to determine the fluid behavior in several revolutionary applications. Specifically, nanoscale surface wetting, nanoscale liquid transport, and nanoscale heat transfer are the most sought-after subjects in recent scientific and industrial applications. This thesis focuses on characterization and possible control of wetting, fluid flow, and heat transfer using nanoscale surface structures. First, wetting behavior on a nanostructured surface was studied to resolve contact angle hysteresis. The droplet was found stabilized at a metastable state with a contact angle significantly different from its equilibrium value due to contact line pinning from the surface asperities. The contact angle was found to increase linearly by increasing droplet size when the droplet is pinned. However, these pinning effects become negligible, and the contact angle reaches the equilibrium value of the corresponding surface when the surface structure size becomes negligible compared to droplet size. Second, fluid flow in nanostructured nanochannels was studied to determine the transport behavior. While the slip boundary condition on a smooth surface correlated with the wetting angle, transport in a nanostructured channel remained mostly independent from wetting condition of the corresponding surface structure. Lastly, droplet evaporation over nanopatterned surfaces was investigated. When the droplet temperature reached the Leidenfrost point, a sudden increase in the interface thermal resistance was observed, which significantly decreased the heat transfer to the droplet. Increasing the size of the surface structure pushed the Leidenfrost point to higher surface temperatures. Current results contribute to various disciplines in engineering and applied sciences.

Keywords and Phrases: *Surface patterning, Molecular Dynamics, Wetting, Pinning, Slip Length, Interfacial Thermal Resistance, Droplet Evaporation, Leidenfrost Phenomena*

ÖZET

NANOYAPILI YÜZEYLERDE MOLEKÜLER DINAMIK SIMÜLASYONLARI ILE NANO ÖLÇEKLI ISLANMA, AKIŞKAN TAŞINMASI VE DAMLACIK BUHARLAŞMASININ İNCELENMESİ

Devrim niteliğindeki birçok uygulamada sıvı davranışını belirlemek için nano ölçekte katı-sıvı etkileşimlerini anlamaya önemli bir ihtiyaç vardır. Spesifik olarak, nano ölçekli yüzey ıslanması, nano ölçekli sıvı taşınımı ve nano ölçekli ısı transferi, bilimsel ve endüstriyel uygulamalarda en çok aranan konular arasındadır. Bu tez, nano ölçekli yüzey yapılarını kullanarak ıslanma, sıvı akışı ve ısı transferinin karakterizasyonu ve olası kontrolüne odaklanmaktadır. İlk olarak, temas açısı histerezisini çözmek için nano yapılı bir yüzey üzerindeki ıslanma davranışı incelenmiştir. Damlacık, yüzey pürüzlerinden temas çizgisinin çivilenmesi (pinning) nedeniyle denge değerinden önemli ölçüde farklı bir temas açısı ile yarı kararlı bir durumda stabilize olduğu bulunmuştur. Damlacık sabitlendiğinde damlacık boyutunun artmasıyla temas açısının doğrusal olarak arttığı bulunmuştur. Ancak, yüzey yapı boyutu damlacık boyutuna kıyasla ihmal edilebilir hale geldiğinde bu çivilenme etkileri ihmal edilebilir hale gelir ve temas açısı karşılık gelen yüzeyin denge değerine ulaşır. İkinci olarak, akışkan taşınma davranışını belirlemek için nano yapılı nanokanallardaki sıvı akışı incelenmiştir. Pürüzsüz bir yüzey üzerindeki kayma sınır koşulu, ıslanma açısı ile ilişkiliyken, nano yapılı bir kanalda taşınma, ilgili yüzey yapısının ıslanma durumundan çoğunlukla bağımsız kalmıştır. Son olarak nano desenli yüzeyler üzerinde damlacık buharlaşması incelenmiştir. Damlacık sıcaklığı Leidenfrost noktasına ulaştığında, ara yüzey ısıl direncinde ani bir artış gözlemlenmiştir ve bu da damlacığın ısı transferini önemli ölçüde azaltmıştır. Yüzey yapısının boyutunun artması, Leidenfrost noktasını daha yüksek yüzey sıcaklıklarına itmektedir. Mevcut sonuçlar mühendislik ve uygulamalı bilimlerdeki çeşitli disiplinlere katkıda bulunmaktadır.

Anahtar Kelimeler ve Deyimler: *Yüzey Desenleme, Moleküler Dinamik, Islanma, Çivilenme, Kayma Uzunluğu, Arayüzey Termal Direnci, Damlacık Buharlaşması, Leidenfrost Olayları*

TABLE OF CONTENTS

LIST OF FIGURES

Figure **Page**

Figure **Page**

LIST OF TABLES

LIST OF SYMBOLS

u,v(t)	Velocity	m/s
y	Distance	m
t	Time	s
a	Acceleration	m/s^2
F,f	Pinning force	N
L	Length	nm
T	Temperature	K
R	Thermal resistance	Km^2/W
q	Heat Flux	W/m^2
t	Time	s
h	Channel height	nm
r	Radius	nm
r(t)	Position	m
R	Radius of droplet	nm
m	Mass	kg

Greek Letters

ε	Interaction strength	eV
θ	Contact angle	deg.
σ	Molecular diameter	Å
γ	Interfacial tension	N/m
τ	Line tension	N
ρ	Density	g/cm^3
δ	Tolman length	

Subscripts

B	Base
C-B	Cassie-Baxter
V	Vapor
L	Liquid
S	Solid
W	Wenzel
∞	Macroscopic droplet
S	Slip
K	Kapitza
E	Energy

CHAPTER 1

INTRODUCTION

The daily usage of nanoscale applications is appealing to a broader use day by day, and accessibility to these applications is becoming more common. The success that normal sized devices cannot achieve can be easily achieved with nanoscale applications. Nonetheless, there are still some physical behaviors in the nanoscale that are not fully understood yet. Particularly in the case of liquid flows, nanoscale fluid behaviors encountered in innumerable revolutionary applications are still not clearly realized. The effects of interactions between solid and fluid have received increasing attention in various fields for engineering and applied science including aerospace, electrochemistry, energy materials, electronics, biomedical, biological membranes, geochemistry, etc. Hence, there is a significant need to understand the physical behaviors of solid-liquid interactions at the nanoscale. However, the investigations of the interactions on a micro/nano scale are rather difficult compare to macro-scale applications because the behavior of fluids at the micro/nanoscale differs from macroscale behavior[1]. In nanoscale flows, the discrete features of the molecular system are not imperceptible with the continuum description. As it is evidently shown in studies that in nanoscale, fluid transport differs significantly from continuum fluid transport due to thermal/viscosity slip, interface/surface force field, and local viscosity[2].

The wettability of the liquid is directly related to the solid-liquid interaction strength. Therefore, it plays an important role in characterizing interfacial phenomena. Research shows that liquid-solid bond strength significantly affects numerous parameters, such as density, velocity, temperature, and pressure[3–7]. The liquid may undergo velocity slip, non-slip, or adsorption, conditional to the strength of the solid-liquid interaction, which has a major impact on flow transport[8,9]. However, such behavior can be identified in the first layer of liquid density instead of the walls because liquid molecules unable to approach the solid walls more than their diameter. The fluid slip plane, influences the apparent height of the channel in the first layer of mobile density near the wall[10].

Despite the fact that nanoscale studies are difficult and costly, molecular dynamics (MD) simulations have proven a valuable and successful approach for providing a context

for nanoscale systems. For these purposes, the molecular modeling of silicone oxide, which is commonly used in emerging technologies[11–13] and water, which is the most found liquid in nature, was carried out in this research. First, molecular dynamics investigations on wetting of nano-patterned silica surfaces are undertaken to examine the influence of nano-sized surface structures on wetting. In this study, as a continuation to wetting on nano-structured surfaces, one of the most unexplained issues of nano-sized wetting behavior, the pinning phenomena is investigated. Six different surface structures are conducted, and they are investigated under hydrophobic wetting condition by determining liquid/solid interactions. There are not enough and fully discovered studies in the literature on the pinning phenomena. Therefore, in this research the characterization of the pinning phenomena and estimation of the equilibrium contact angle without the contact angle hysteresis is established. Second, force-driven water flow via surface patterned silica nanochannels is simulated utilizing non-equilibrium molecular dynamics (NEMD). The slip behavior of the transportation of water in silica nanochannels at a confined channel length is estimated for designed surface patterns. The impact of the roughness effect on the slip behavior was investigated by altering the surface nanostructure. The diversity of surface structures is connected to slip length, and nano-sized surface structures generated on the surface have been proven to affect the slip behavior. The solid-liquid interactions which determine the velocity slip can also determine the surface wetting dynamics. Therefore, velocity slip and the resulting fluid transport can be predicted or even controlled by wetting dynamics or contact angle. Thus, the slip behavior for the differently designed surface structures is compared with the measured contact angles on these structured surfaces by using the proposed theories. Third, nano-level transient heat transfer studies are carried out by conducting droplet evaporation studies on the four most critical of the previously mentioned nano-patterned surfaces. The characterization of the interface thermal resistance is studied on these models. In addition, by determining the effects of nanopatterning on droplet evaporation, the occurrence of the vapor layer at the interface of solid-liquid systems, which can be called the Leidenfrost phenomena, is investigated. Also, the variation of interfacial thermal resistance according to the Leidenfrost phenomenon was investigated and the relationship between them was determined.

1.1. Wettability

Surface wetting plays a significant role in multiple applications. Wetting is a crucial concept that describes the capacity of liquids to retain contact with a solid surface, which is coming from intermolecular interactions between solid and liquid atoms or molecules of similar and dissimilar types. The wettability of a surface is determined by the balance of adhesive and cohesive forces. Wetting is the process of combining the three phases of a material: gas, liquid, and solid. At the interface of each phase, interfacial tension occurs due to excess energies resulting from a force imbalance. When these interfacial tensions in equilibrium, the surface wetting can be determined. The angle between liquid-vapor interface and solid-liquid interface is known as wetting or contact angle which can be seen in Figure 1.1.

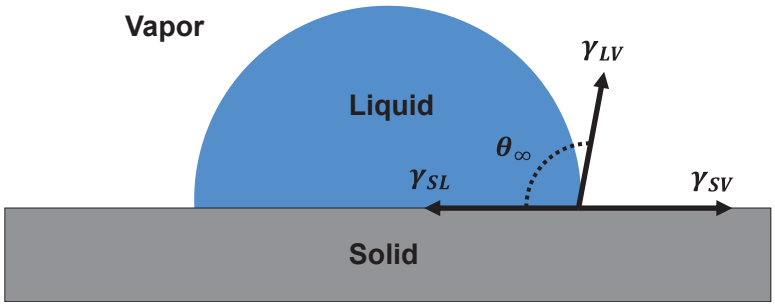

Figure 1.1. Representation of contact angle and surface tensions between each phase.

The surface wettability can be determined with the Young's equation as well as it is used to determine the interfacial tension between different phases. It can be found as,

$$\gamma_{SV} = \gamma_{SL} + \gamma_{LV} \cos\theta_\infty \tag{1.1}$$

where the solid(S), liquid(L), and vapor(V) surface tensions between phases are γ_{SV}, γ_{SL}, and γ_{LV}, respectively. θ_∞ is the wetting angle at macroscopic scales. When the surface tension between phases is perpendicular to each other contact angle becomes 90^0 to the surface. If the angle is higher than 90^0, the surface is called hydrophobic for the water-type liquid. If the wetting angle is lower than 90^0, the surface wettability is hydrophilic for the water-type liquid. Additionally, if the surface has an angle as high as 120^0 or

above, the surface is called superhydrophobic for water substances. When the surface free energy gets lower, the degree of wetting decreases.

The lotus flower is associated with cleanliness and purity in Asian cultures. Because of its hydrophobic surface properties, lotus leaves repel water. The micro-sized surface structures can explain the hydrophobic nature of the Lotus leaf. Since the discovery of the lotus effect[14], surface patterning has begun to be implemented to control the wetting behavior of the surfaces[15]. The hydrophobic characteristic of lotus leaf is a biomimicking example of the nanoscale surface roughness and is an important concept for wetting behavior. The discovery of the lotus effect has influenced to predict two different approaches for wetting on patterned surface structures as Figure 1.2. illustrates this. The Wenzel model is one of the approaches that describes a rough surface with chemical homogeneity which droplets are penetrated the rough structures leading to high adhesive forces[16]. Diversely, in the second approach Cassie-Baxter (C-B) model assumes a rough surface with chemical heterogeneity as in water stays on top of the surface structures and not penetrable[17].

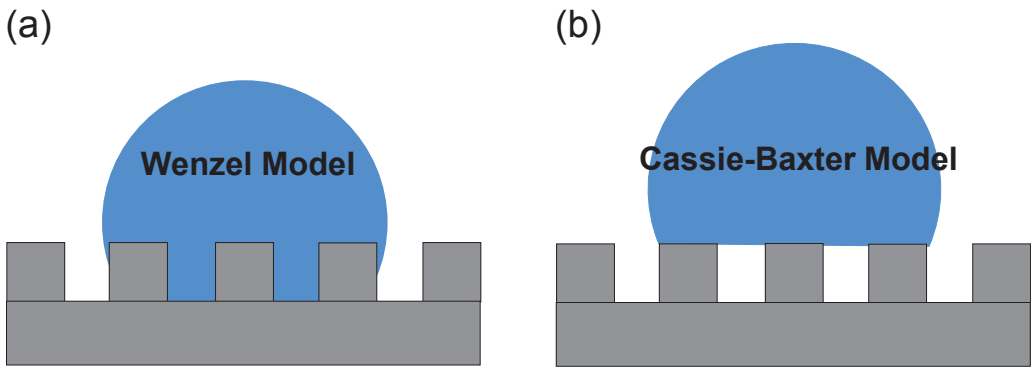

Figure 1.2. Wenzel and Cassie-Baxter models.

For the investigation of the wetting on nanoscale surface roughness, the hierarchical wetting should be considered both for micro and nano size. The hierarchical wetting can be observed for Wenzel and Cassie-Baxter models that each model is divided into two section as micro and nano size wetting[18] which can be seen in Figure 1.3. In Figure 1.3, part (a) describes the Wenzel-Wenzel model, while part (b) describes the Wenzel-Cassie Baxter model. Additionally, the Cassie-Baxter-Wenzel model is explained in part (c), while the Cassie-Baxter-Cassie-Baxter model is shown in part (d). Investigation of primary micro and secondary nanoscale structures has excellent importance for nanoscale droplet studies.

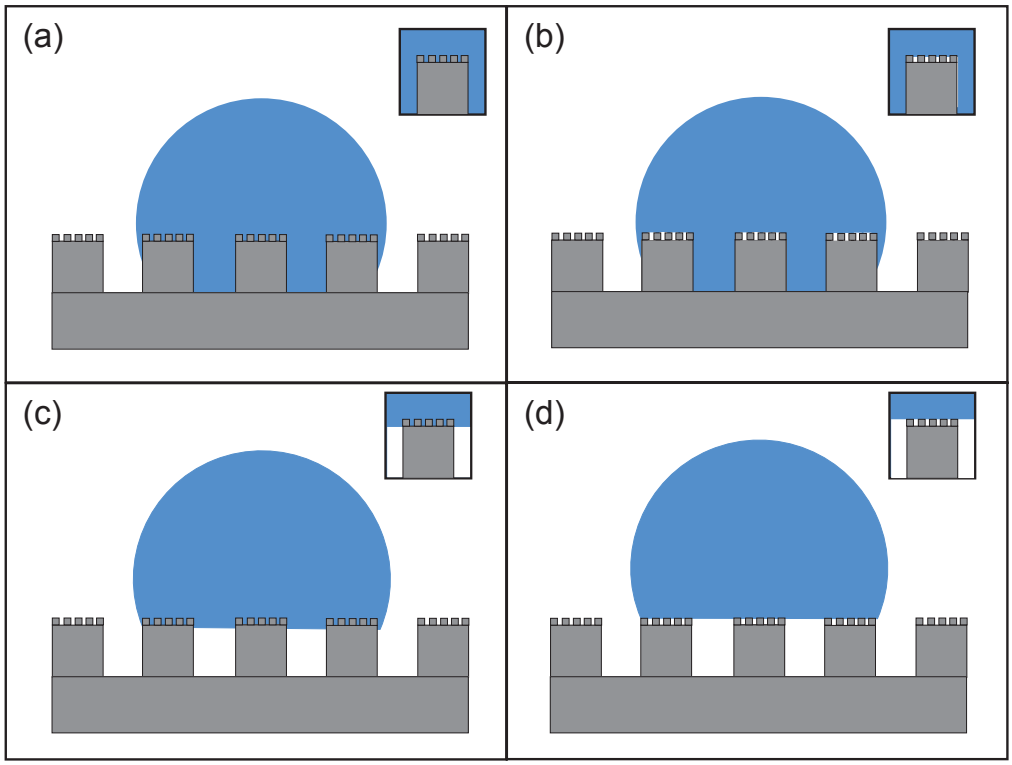

Figure 1.3. Hierarchical wetting behavior for both nano and micro size for Wenzel and Cassie-Baxter states.

Lotus leaves are hydrophobic surfaces; droplets on the lotus leaf slide down and do not stay on the surface; this is due to low adhesive forces. However, in the rose petal effect[19], micro/nanostructures on the surface give hydrophobicity, but the surface is highly adhesive. The primary microstructures and secondary nanostructures o lotus leaf and rose petal can be seen in Figure 1.4. The reason for the sticky behavior of the rose petal is dual wetting dynamics. While water droplets do not fill the gaps in the surface roughness at the micro-scale, water molecules at the nanoscale fill the gaps in the surface roughness. For this reason, droplets do not slip, and a sticky behavior is observed on the rose petal. This rose petal effect is defined as 'impregnating Cassie-Baxter state'. Adhesive forces keep the drop from falling out, which clearly shows the significance of nanoscale wetting. Thus, nanoscale wetting is important to resolve hierarchical wetting mechanisms.

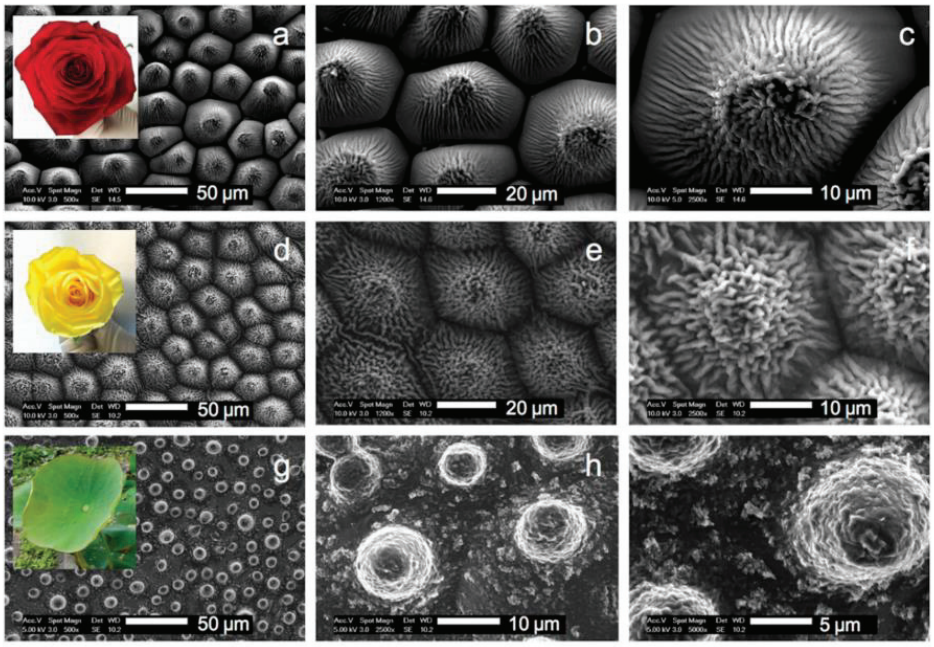

Figure 1.4. Primary microstructures and secondary nanostructures on lotus leaf and rose petal[20]

1.1.1. Wetting at Nanoscale

In nanoscale droplets, the interfacial tension between each phase is found to be inadequate for explaining the wetting behavior. When the liquid-vapor interface tension varies due to curvature at the interface and Tolman length[21], the three-phase (solid, liquid, and gas) line tension[22] becomes important for nano-sized droplets, and these effects should not be neglected. Therefore, to characterize the effect of line tension with Tolman length, modified Young's equation given as,

$$\gamma_{SV} = \gamma_{SL} + \gamma_{LV}\left(1 - 2\frac{\delta}{R}\right)\cos\theta + \frac{\tau}{r_B} \tag{1.2}$$

where terms θ, τ, and r_B refers to nanoscale contact angle, line tension, and base radius of droplet, respectively. The solid(S), liquid(L), and vapor(V) surface tensions for Young's equation is given and γ_{SV}, γ_{SL}, and γ_{LV}. δ is the Tolman length, and R is droplet radius. The inequality of intermolecular forces on three-phase lines and the interactions between surfaces can be described as line tension and Tolman length. Tolman length can

be defined as a measurement how much the surface tension of the small liquid drop differs from its planar value. Thus, as the droplet size decreases, the surface tension decreases. Ultimately, there can be quite a significant reduction for the small droplet sizes. The determination of the line tension for a specific value of the small size droplets, particularly for the patterned surfaces, remains a challenge. It is standard procedure in MD to model big enough and cylindrical droplets to extract line tension and Tolman length effects from nanoscale measurements. Also, when the droplet is modelled as cylindrical, the length of the contact line does not depend on the droplet form.

1.1.2. Wetting Hysteresis

In practice, achieving a unique contact angle for heterogeneous surfaces is almost impossible. A couple of factors affect contact angle hysteresis, such as surface roughness, surface deformation, chemical heterogeneity, etc. Due to pinning of the contact line of the droplet, the wetting behavior is subject to contact angle hysteresis. Thus, the different contact angle results than equilibrium values can be obtained for heterogeneous surface. Although chemical heterogeneity and surface defects are known to affect contact angle hysteresis, it has been experimentally proven by Ramos et al.[23] that these effects are not similar. The contact angle of a sessile droplet is typically measured within a range specified by the advancing and receding angles, rather than as a single value. The maximum and minimum contact angles without changing the solid-liquid interfacial area are defined as advancing and receding angles; this means that they are measured shortly before the contact line moves. The difference between advancing and receding angles is named contact angle hysteresis. Unlike the flat surface, with the surface heterogeneity, the pinning effect causes the base of the droplet to remain constant while it increases the apparent contact angle, as can be seen in Figure 1.5. The contact line of droplet needs to overcome an energy barrier caused by the pinning force in order to move from one pattern to the next[24]. When the droplet volume rises, the contact line pin to the structures, which might cause the wetting angle to increase or decrease. Afterwards, The contact line is moved to the neighboring pattern, causing contact angle to change again[25].

Considering this information, it can be understood that rough surface wetting is different from the wetting of the planar surface. The Cassie-Baxter and the Wenzel assumptions are not enough to explain the rough surface contact angle behavior.

Therefore, based on the rough surface to droplet size ratio, the contact angle changes significantly for the same solid-liquid interface area. The contact angle advances or recedes subject to volume of the droplet without changing its base radius, or the contact angle varies for a constant volume with changing its base radius. The literature shows that this behavior is explained with different theories. The first one is calculating the pinning force which occurs on the edge of the pillars due to the heterogeneity of the solid surface[24,26–28]. The other approaches are mainly focused on the modification of the Cassie-Baxter and Wenzel models. The calculation of the free energy between the solid-liquid interface the Cassie and Wenzel states is modified[29,30].

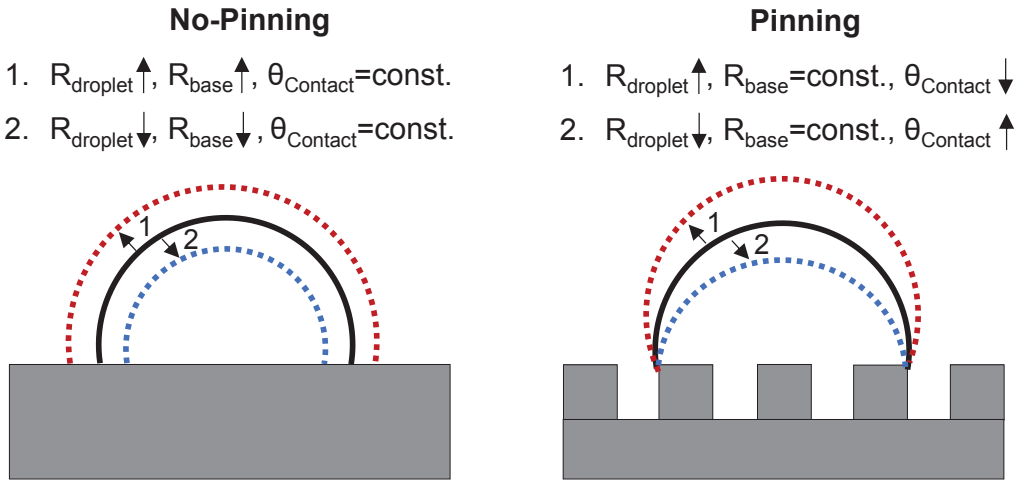

Figure 1.5. Contact line pinning and no-pinning during droplet volume change.

Hong et al.[31] found that when the attractive force between surface and liquid gets more substantial, the contact angle hysteresis gets larger. Another study by Reyssat and Quéré[32] examined contact angle hysteresis with pillared surfaces in Cassie state. They discovered that contact angle hysteresis gets stronger with increasing pillar density. They also stated that the hysteresis is not dependent on droplet volume.

According to new study, substrate heterogeneity induced pinning effects impacts line tension determination using the revised Young equation[26]. This stabilizing effect has an impact on the wetting conditions and alters the contact angle of the droplet. Furthermore, considering the pinning effect of wetting states, Zhang et al. updated Young's equation to produce contact angle as follows,

$$\cos\theta = \cos\theta_{\infty} - \frac{\tau}{r_B \gamma_{LV_{\infty}}} - \frac{f_{pin}}{2\pi r_B \gamma_{LV_{\infty}}} \tag{1.3}$$

where τ, r_B and f_{pin} refers to as line tension, base radius and the pinning force, accordingly. Also, another research[28] reveals the pining forces as,

$$F_{pin} = \gamma_{LV_{\infty}} \left(\cos\theta - \cos\theta_{\infty} \right) \tag{1.4}$$

where the equilibrium contact angle and the dynamic contact angle are θ and θ_{∞}, respectively. The findings of the research demonstrate that the wetting behavior of structured surfaces is dominated by localized liquid-solid interaction around the contact line, implying a molecular basis for the pinning force.

1.2. Fluid Transport

Micro/nanofluids is interested with the behavior of confined fluids on a small scale. Also, it controls, and manipulates these behaviors. Lately, nanofluidic has drawn significant interest, thanks to the growing interest in developing quicker, smaller, and more efficient equipment. Nanoflows, which are fluid flows in nanometer-scale channels and pores, are crucial in defining the functional properties of many biological and technical devices and systems. Surface tension, energy dissipation, and other variables can cause fluids to behave differently at the nanoscale than they do at the macroscale. Fluidic resistance begins to dominate systems at the nanoscale level. In contrast to negligible effects in macroscopic channels, the significance of the surface and the dimensional effects of molecules on fluid transport must be thoroughly understood in nanochannels. Density variations at the interface can be substantial in nanoflows but are generally insignificant at higher scales. In confined nanoflows, transport characteristics such as diffusion coefficient and viscosity[2] may differ. The interaction of the fluid with the surface (hydrophilic and hydrophobic, for example) can significantly impact the flow characteristics of nanochannels. At nanoscales, the concept of boundary conditions at solid-liquid interfaces is still remaining unclear.

1.2.1. Slip Boundary Condition

Although its existence has been discussed for a long time, slip condition has been found to be very important in nanoscale. In 1784, Coulomb conducted the first experiment on a solid surface to verify the no-slip boundary condition, concluding that it was true even at microscopic sizes.

Navier proposed the concept of velocity slip for the first time in 1823. The surface velocity is equal to wall shear stress when compared to the well-known Navier boundary conditions[1]. The velocity slip can be defined as,

$$u_{slip} = L_s \left. \frac{du}{dy} \right|_{@wall} \tag{1.5}$$

In this equation, u_{slip} is the slip velocity, L_s is the slip length, the term seen in the form of *du/dy* is the velocity gradient at the wall. The slip length is a hypothetical distance over which the slip velocity approaches zero. The duration of the slip is anticipated to be determined by the solid-liquid bonding characteristics as well as flow dynamics.

The effect of the wall structure also has a special significance in nanoflows. Cao et al.[33] has revealed that the surface roughness have an influence on surface wettability and boundary slip. Especially, the nanostructured surface can exhibit superhydrophobicity and result in large velocity slip of the nanoflow. Sofos et al.[34] shows that the size of the cavity influences the fluid atom localization, and its impact affects the velocity values within the cavities. Then, the slip length along the surface is reduced. Cottin-Bizonne et al.[35] showed that different pressures substantially change how surface nanostructures reduces slip length and friction on the surface. According to Vinogradova and Belyaev[36], microstructures and nanostructures enhances the hydrophobic slip. On the one hand, some studies showed that surface structures reduces the slip length[37,38]; however, another examination reported that surface structures enlarges the slip length[39].

The effects of volume forces, which dominate fluid characteristics at the macroscale, are diminished at the nanoscale, while the effects of surface forces are amplified. Since surface forces become dominant in nanoscale flow, surface wetting has a major influence on how the flow occurs. The influence of wettability on slip length is studied by many researchers. In general, it was discovered that the hydrophilic surfaces

generate no-slip boundary condition, whereas hydrophobic surfaces dominate the velocity slip[5,33,40–42]. The researchers found that the surface roughness reduces the slip length when the surface is in the Wenzel state[43]. However, when the surface is in the Cassie-Baxter state or the intermediate state (between Wenzel and C-B states), the surface roughness increases the slip length due to vapor trapped between the surface structures[44,45].The nanoscale fluid flow depends sensitively on the slip length and the contact angle. Voronov et al. reveals that the longer the fluid contact with the wall, the greater the slip length and the less the contact angle becomes[4]. The theory created by Huang et al. has been shown that the slip length can be associated with the contact angle[41]. In the Young's equation, the Laplace estimation of the interfacial tension and the solid/liquid interaction energy relationship can be combined to determine the relationship between the contact angle and the slip length as,

$$L_s \sim (1+\cos\theta)^{-2} \tag{1.6}$$

With addition to the equation by evaluating the limits of $1+\cos\theta$ term, Sender et al reported that the same equation can be collapse into[46]

$$L_s \sim (180-\theta)^{-2} \tag{1.7}$$

Yen and Soong[47] investigated using MD simulations that surface wetting and flow dynamics are influenced by surface patterns and the theory is mentioned in Eqn. (1.6) was found to be associated only with Cassie-like rough surfaces. For comparison, Wenzel-like nanostructure cases, they stated that slip boundary conditions cannot be related with contact angle results. Alvarado et al.[48] also studied the theories and showed that the results are a better fit for Eqn. (1.7) than Eqn. (1.6), and they said that slip length highly depends on solid density. The influence of solid molecular density on the slip length was also mentioned by Sokhan et al[49]. Cho et al.[42] investigated the influence of liquid polarity on slippage and found out that for polar liquid, wettability does not have a significant influence on slip length. They also stated that equation (1.6) applies to the non-polar liquids. With the gathering all the data available from literature, Kalyoncu and Barisik[50] show the relation between the slip length with the wetting. Their results were also

compared with the theories mentioned in equation 1.6 and 1.7 which can be seen in Figure 1.6.

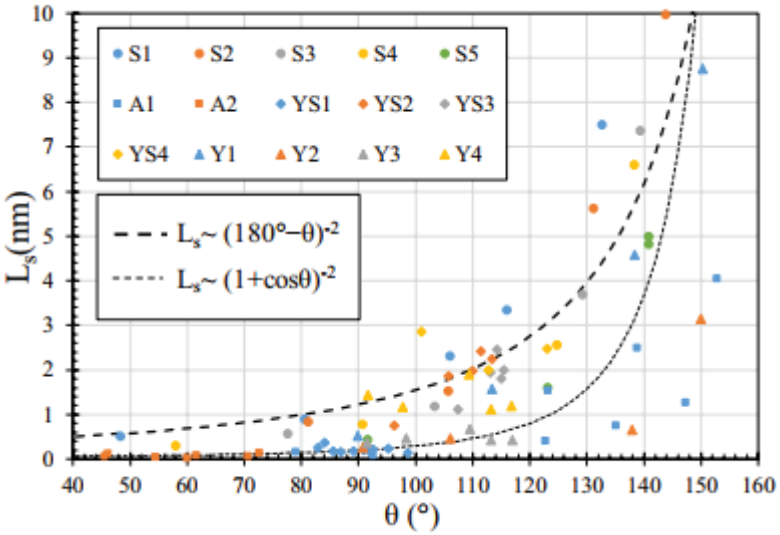

Figure 1.6. The relationship between contact angle and slip length with data obtained from literature and the proposed two theories[50].

Although neither model can calculate the results of a particular situation, they discovered that they are fairly good at predicting the overall behavior of slip length and contact angle. They stated that Huang et al. has a better consistence for hydrophobic cases ($\theta \leq 90$), whereas Sender et al. has a better consistence for the hydrophilic cases ($\theta \geq 90$). In this thesis, one of the aims is to correlate the result with these proposed theories.

1.3. Heat Transfer

Heat transfer is primarily influenced by temperature and heat flow. The quantity of thermal energy accessible is determined by temperature, and heat flow is the movement of thermal energy. As the industrial capacity and the world's energy demand grow each day, heat transfer studies are becoming more common and significant. Heat transfer advancements improve energy efficiency and extend the life of materials by shortening processing times. The development of nanoelectromechanical systems and the miniaturization of microelectronic device components necessitates a better understanding of thermal transport in nanomaterials, in which the atomic structure of matter becomes so crucial that the validity of well-known continuum approaches is called into question[51].

Small-scale devices subjected to intense heat in various areas, such as aerospace, biomechanics, electronic components, and laser applications, now require intense cooling resolutions. Heat transport in these devices should be designed efficiently, and as the scale gets smaller every day, more precise heat calculations are necessary. That is why heat transfer characterization in nanoscale is a critical issue. Heat transfer at the macroscale and at the nanoscale are two distinct study areas. Classical heat transfer equations may not be sufficient in nanoscale situations[52], and new ways to describe heat transport at the nanoscale will be required. Thermal transport across the solid-fluid interface is another important aspect of nanoscale heat transfer, which is important in a variety of applications.

1.3.1. Interfacial Thermal Resistance

Because continuum theories are unsuitable in nanoscale heat transport investigations, interface thermal resistance is effective. It should be emphasized that thermal boundary resistance differs from contact resistance, and interface thermal resistance is defined as a temperature discontinuity between dissimilar materials. The temperature jump is the result of mismatch in the phonon scattering of the materials forming the interface. Traditional models of phonon scattering can estimate the upper and lower limits of interface thermal resistance (ITR), but to fully understand interface phonon scattering mechanisms, a complete examination of intermolecular interactions is necessary. Thermal resistance can explain temperature jumps seen between nanoscale interfaces. In heat transfer research, Kapitza[53] denoted the influence of the interface resistance length at the solid/liquid interface, and thus ITR can be ascribed to as Kapitza resistance (R_K), as can be seen in equation 1.8.

$$\Delta T = -R_K \, \vec{j} \cdot \vec{n} \tag{1.8}$$

Here, ΔT, $\vec{j}$, and $\vec{n}$ represent temperature jump, heat flux and wall normal, respectively. The interface thermal resistance (ITR or R) may be expressed as follows for a simplified version,

$$q = (T_{solid} - T_{liquid}) \frac{1}{R} \tag{1.9}$$

In heat transport systems between the two walls, the heat flux applied to the interface of two incompatible materials is used to calculate the Kapitza length (L_K), which can be used as an alternative to Kapitza resistance, which provides some indication of near-surface physical processes and can be calculated as follows,

$$\Delta T = L_K \left. \frac{\partial T}{\partial n} \right|_{@liquid} \tag{1.10}$$

where ΔT is the temperature difference between solid and liquid, $\partial T / \partial n$ is thermal gradient on the liquid.

1.3.2. Droplet Evaporation and Leidenfrost Phenomena

Droplet evaporation occurs until the vapor pressure surrounding the droplet reaches its saturation point. The study of droplet evaporation has gotten great interest because of its importance in many applications as cooling, printing, coating, etc. Due to specific utilization areas, for example inkjet printing[54], micro/nanofabrication[55], and the development of new optical and electrical materials[56], the field has lately grown in popularity. To understand the link between droplet evaporation systems, a substantial amount of experimental[57–59] and theoretical[60–63] research has been done. Around 100 years ago, Maxwell presented the results of early theoretical attempts on droplet evaporation, in which he postulated that mass transfer controls the evaporation process[64]. Droplet evaporation ideas have evolved and improved since then. Three droplet evaporation models were created based on contact angle and contact line dynamics. In the constant contact angle model[65–67], the three-phase line moves while evaporation continues, but the contact angle remains the same. In the constant contact line model[58,65–67], the three-phase line remains constant while the contact angle diminishes throughout evaporation. In the mixed model[65], both the contact angle and the contact line change.

When a droplet evaporates, a vapor layer can develop at the interface, which is an essential component of droplet evaporation. Thus, the hovering drop reaches the

Leidenfrost condition, resulting in a Leidenfrost drop[68]. Leidenfrost droplets are also seen in everyday life. For example, chefs sprinkle water droplets on a hot pan to see if the temperature of the pan has risen enough. In the Leidenfrost state, the heat transmission only happens not only by conduction but also by radiation because the vapor layer eliminates liquid-solid contact. In the Leidenfrost regime, a weak heat transfer occurs because the heat transfer capacity of the vapor layer is low. As a result, suppressing the Leidenfrost state for the purpose of improving heat transmission is a great interest.

When evaporation occurs at the liquid-solid interface, it is called boiling. Droplet evaporation can be divided into four regions, as can be seen in Figure 1.7. When the lifetime of the droplets is shown with increasing wall temperature, different regions of droplet evaporation can be identified. In the first region, the droplet is in a single-phase regime. The evaporation only occurs at the liquid-vapor interface. When the surface temperature continues to increase, after a certain point, the droplet goes to the onset of the nucleate boiling regime. Two different flow regimes occur in this region. In one regime, small bubbles begin to form at the solid-liquid interface and separate the surface from the liquid. On the other hand, in another regime, some parts of the liquid droplet still keep in contact with the surface and heat transfer takes place only due to this solid-liquid direct contact. As the surface temperature increases further, the temperature exceeds the critical heat flux point and enters a transitional boiling regime. In this regime, bubble formation is very rapid and surface conditions alternate between nucleate boiling and film boiling. Vapor layer formations begin to appear in some parts of the surface. Eventually, continued temperature increases reach the film boiling regime, and the point at which the film boiling regime begins is called the Leidenfrost point (LFP), where heat flux is minimum. In the Leidenfrost regime, the droplet's contact with the surface is completely cut off due to the formation of the vapor layer. Heat transfer from surface to liquid in this region only develops due to conduction and radiation through vapor. Water droplets on top of the vapor layer slowly evaporate and the droplet moves around. With the increasing surface temperature, radiation heat transfer becomes even more significant and heat flux increases.

Surface chemistry and surface structure have been implicated in solid-liquid interfacial heat transfer in several studies. There is a great interest to explore the impact of surface structure on solid-fluid interfacial heat transfer because of recent developments in micro/nano fabrication methods. Surface characteristics such as wettability, roughness, and porosity have long been recognized to have a significant influence on the thermo-

hydrodynamics of droplet evaporation dynamics[69]. Customize LFP in the past, several surface wetting materials characteristics were utilized. Although surface roughness has a significant impact on surface wettability[70], its impact on the Leidenfrost effect is also dependent on the roughness elements' ability to reestablish liquid-solid contact[71]. It is mostly agreed opinion for the Leidenfrost phenomenon, when the surface roughness increases, the liquid-solid contact maintains longer due to penetration of the roughness element through the vapor layer. In order to separate the liquid-solid contact, a larger vapor layer is necessary as the surface roughness increase, thus leading to higher LFP.

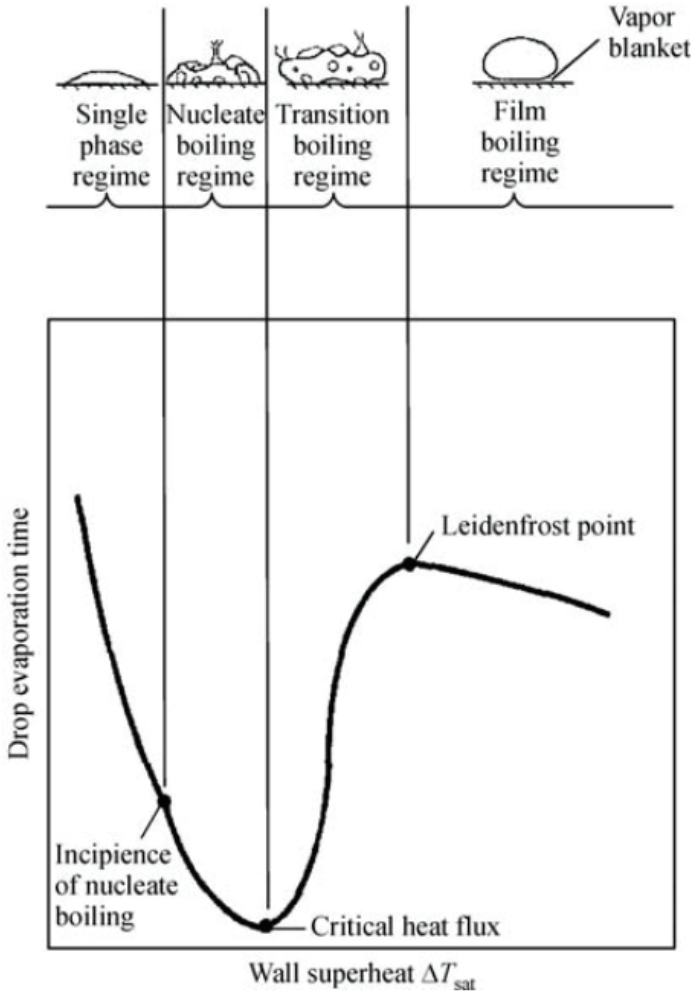

Figure 1.7. The drop's lifetime and heat transfer regimes at various wall temperatures[69].

Many studies have been carried out to investigate the effects of micro and nanoscale roughness effects on Leidenfrost. The majority of these studies were carried out using microsize droplets. In most of the studies, the effect of the vapor layer on boiling

was tried to be reduced with micro/nanoscale surface structures. Therefore, it was desired to move the Leidenfrost point to higher temperatures. Kim et al.[72] were among the first ones to study Leidenfrost phenomenon on the surface of micropillars. The results show that the LFP increased for both Au and SiO_2 coated micropillar surfaces compared to flat surface. Kwon et al.[73] also studied effect of micropillar surfaces on LFP. Their results also indicated an increase of LFP for micropillar surface. They found out that the micropillar structures affect the droplet dynamics and said that increase in LFP was greater in sparse spacing compared to dense spacing. However, one study conducted by Arnaldo del Cerro el al.,[74] LFP is reduced with micropillar structured surface. This reduction is assumed due to rapid formation and development of bubbles. Later, Tran et al.[75] examined the LFP according to the height and pitch of micropillars. As a result, they concluded that as the height of micropillars increases, the LFP decreases compared to the flat surface due to the heat transfer area increases with increasing pillar height and the vapor film between the droplet and the hot surface becomes trapped. In one of the studies that followed, Park et al.[76] studied the width, height, and pitch of micropillar structures together to characterize the variation LFP temperature. Their results show that LFP increased with increasing pitch size. However, it decreased with increasing width size.

Although there is much evidence that LFP changes when flat surface and micro structured surfaces are compared when studies are examined, the increase or decrease in LFP differs according to width, pitch, and height, even though it is accepted that many studies have been done on this subject, no definite conclusion has been reached on how LFP changes with surface structures.

The Leidenfrost effect has been well investigated for macroscale applications such as cooling[72], liquid transport[77], and drag reduction[78]. Also, as mentioned above, it has received a lot of attention at the microscale, but it still requires further research at the nanoscale. It is very important to analyze the Leidenfrost phenomenon in the nanoscale regime. However, since the experimental analysis of nanodroplets is below optical resolution, molecular modeling is required to analyze nanoscale droplets. Depending on the droplet's initial size, nanoscale droplets exhibit extraordinarily rapid evaporation dynamics. In addition, to examine the LFP effect at the nanoscale, how this effect changes according to the nanoscale heat transfer phenomena should also be examined. Therefore, it should be found out how the LFP changes concerning the interfacial thermal resistance (R).

1.4. Molecular Dynamics Simulation

Molecular dynamic studies have played a significant role in explaining nanoscale studies due to the broadening increase in nanoscale applications. The complicated and expensive laboratory setups of small systems are the main reasons why molecular dynamic studies are becoming essential.

Alder and Wainwright[79] developed the molecular dynamics approach to study atom interaction in many-body structures in the late 1950s. Following that, Rahman[80] achieves a practical ability for simulating liquid argon in 1964. His system has 864 particles using the Lennard Jones (L-J) potential by applying Newton's equation of motion.

Molecular dynamic simulations govern with Newton's Law of motion by modeling every atomic and molecular motion in a system. Due to quantum mechanical phenomena, each atom in MD is treated as a point mass and exposed to force fields, which are described by potential functions. The molecular forces that other atoms exert on each atom are then measured. The net force on the atoms is calculated and Newton's 2nd Law is applied to find their atomic trajectories in each time interval.

The first step in molecular dynamics is to determine the atoms and their positions in the system. Afterward, the domain of the system is defined, and because of the infinitely small dimensions, a periodic boundary condition is customarily used. Then, to catch interatomic interactions, potential functions are established. Finally, the system is processed in terms of ensembles and time integration.

1.4.1. Fundamentals of Molecular Dynamics

The basic dynamic properties of each atom or molecule, such as position, velocity, and interaction forces, are determined using molecular dynamics (MD) simulation. After that, statistical methods are used to get macroscopic physical parameters like pressure, temperature, and volume. As mentioned before, the origin of MD simulations is Newton's second law, as shown in equation 2.1, which states that all forces are balanced.

$$F_i = m_i \frac{d^2 r_i}{dt^2}, \qquad (i = 1, 2, 3, ..., N) \tag{1.11}$$

Where F_i, m_i, r_i, and t represents the atomic force, mass of an atom, position vector of the atom, and time, respectively. Velocity is calculated by integrating equation 2.1 over time once, and displacement is calculated by integrating twice. The velocity profile equation must be solved using initial states to gain more information about the motion of each molecule in the system. The equation of the velocity profile can be developed using time and space averaging methods[81]. Some of the molecules in the simulation may have a complicated interior geometry. Instead of Newton's 2nd law, an extended Newton's equation can be utilized in this circumstance. However, the simulation procedure remains the same. Determining the dynamic parameters of the molecules, the equation of motion is first integrated once or twice, and then averaging techniques are applied to the dynamic parameters. Physical parameters can be obtained in this manner.

In modeling, it is critical to comprehend events and capture system characteristics using physical rules and with the least amount of calculation time. Because there are so many potentials for atoms in molecular dynamics, it's important to get it right. Pairwise and multibody potentials are the two types of potential functions. Pairwise potentials are normally preferred due to processing costs, although multiple body potentials are necessary for situations where pairwise potentials are insufficient to simulate.

To represent dispersive interactions between atoms, the Lennard-Jones (L-J) potential is often employed. In the L-J potential, the distance at which potential becomes zero is essential, and it is also known as particle diameter. The atoms act attractive when their distance is greater than their diameter, the L-J potential is negative, while the atoms act repulsive when their distance is lower than their diameter, the L-J potential is positive. The L-J potential is referred to as a 6-12 potential since it includes exponential 6 and 12 terms which can be given as

$$E_{LJ} = 4\varepsilon\left[\left(\frac{\sigma}{r}\right)^{12} - \left(\frac{\sigma}{r}\right)^{6}\right] \tag{1.12}$$

where σ, ε and r terms represent the atomic diameter, interatomic energy between atoms and interatomic distance, respectively. With a deeper well depth, the interaction between two particles becomes stronger.

In a system including ions or molecules with electric charge, electrostatic interactions are computed. For certain compounds, electrons are drawn to elements with a larger proton number, resulting in polarization. Partially charged molecule components are allocated to model polarization. It's worth noting that even if polarization is detected, total net charge equals zero. As a result, the total of partial charges should be zero. Electrostatic interactions may be divided into two types: short-range and long-range. To mimic electrostatic interactions at a small distance, Coulomb's law is employed. The L-J equations are often modified by adding different electrostatic interaction. Long-range electrostatic potentials are significantly more difficult to apply and take a lot of time to compute. PPPM (Particle Particle Particle Mesh) and Ewal Summation are the two most common long-range electrostatic interaction functions. Because of its computational efficiency, the PPPM method is used in this work. PPPM firstly maps the charges in three dimensions before using the three-dimensional fast Fourier transform to determine the Poisson equation on the meshes. To detect long-range electrostatic interactions, the electric field over the networks is interpolated[82]. Describe the bulk structure of substrates and reflect the physics of the underlying processes; complicated potential functions are necessary, which are more complex than two-body potentials. For certain atoms, such as the silicon potential established by Stillinger and Weber[83], or in specific forms and characteristics adjusted for particular systems, several body potentials may be generated. Tersoff potential, for example, is usable for Si, SiC, and SiCGe systems. Munetoh et al.[84] modified the Tersoff potential for silica structures, which was originally suggested for silicon structures.

Due to the complexity of water, numerous molecular dynamics-based water models have been created to reflect its physical properties. There is, however, no model that can represent all water characteristics. As a result, water models should be chosen based on the qualities that are necessary for capturing. TIP3P[85] , TIP4P[85], SPC[86], and SPC/E[86] are some of the most often utilized water models in the literature. Short range dispersion forces are often required to create thermodynamically stable water models. These models differ in the partial charges subject to the O and H atoms. The different water models also vary in the bond length and bond angle between O-H-O atoms. Due to the high computing requirement in MD, it is not efficient to model the system bigger than nanometers, thus several approaches are used to decrease the computational effort and produce time-efficient simulations. Fixing non-interest-related characteristics and lowering computing costs is one of the most frequent techniques. Ensembles of particles

are produced in order to do this. As a result, ensembles are necessary in molecular dynamics simulation. The ergodic hypothesis inspired the ensemble averaging approach, which is used to acquire desired particle characteristics. Essentially, this theory states that when the particle's time-dependent activity is averaged long enough, extracted characteristics may be utilized to replace macroscale behavior. The characteristics of systems such as pressure, temperature, energy, etc. are maintained constant to form an ensemble. The most familiar ensembles used in MD are NVE, NVT, and NPT.

In microcanonical (NVE) ensemble, pressure and temperature varies while total particle number (N), total system volume (V) and energy (E) is fixed. There is no heat transmission between the system and the environment in microcanonical ensembles. In canonical (NVT) ensemble the total number of particles (N), volume (V), and temperature (T) of the system are conserved. Isothermal and isobaric (NPT) ensembles are employed with variable heat transfer and volume, other properties are conserved. Thermostats are used in NVT and NPT ensembles to maintain a consistent temperature. The Nose-Hoover thermostat, Berendsen thermostat, and Anderson thermostat are the most used ones.

To overcome the convergence problems in MD simulations, it is highly important to assign initial conditions correctly. The locations of the atoms are calculated in each time step to identify the time-dependent behavior of the atoms. The atom position, velocity and acceleration are all taken into consideration when determining the location of the atoms every time step. The Boltzmann distribution is used to allocate particle velocity at the start of the simulation. To capture time-dependent features of the system, efficient time integration algorithms are created. Taylor expansion is commonly used to estimate the unknown value of a function by using its derivates at a given moment. The position is determined by r(t), and first-time derivative is denoted by v(t). The time derivative of the velocity function may be used to calculate acceleration, a(t). For a given moment t can be denoted as time, and δt can also be denoted as a time step. Thus, Taylor expansion may be written for the position at that time t + δt, r(t + δt),

$$r(t+\delta t) = r(t) + \frac{v(t)}{1!}\delta t + \frac{a(t)}{2!}\delta t^2 ... \tag{1.13}$$

The velocity at that time t + δt, v(t + δt) and acceleration at that time t + δt, a(t + δt) by using Taylor expansion can be found as

$$v(t+\delta t) = v(t) + \frac{a(t)}{1!}\delta t + \frac{b(t)}{2!}\delta t^2 ... \tag{1.14}$$

$$a(t+\delta t) = a(t) + \frac{b(t)}{1!}\delta t + \frac{c(t)}{2!}\delta t^2 ... \tag{1.15}$$

1.5. Molecular Modelling of Silica

We used silicon dioxide, commonly known as silica, in our study because it is one of the most abundant substances in nature. Silica is also used in a variety of applications such as micro/nanofluids[87], energy[11] and industrial[88] applications, and microelectronics[89]. Thermal oxidation causes thin silica films to form spontaneously on silicon wafers. Thus, if we talk about any silicon surfaces, we need to examine the silica behaviors due to this oxidation. Because of the widespread interest, many studies have been conducted on modeling silica structures with computer simulations. The molecular dynamics (MD) method has been widely used to find silica properties at the molecular level. As it's done in many studies[90,91], β-cristobalite form of silica was used for the simulations due to the similarity in molecular properties with amorphous silica and it's easier to modify for the structured surface creation. For the silica intermolecular interactions, we used multibody Tersoff Potential[84,92]. For the water model, SPC/E water model is employed in simulations. By using the SHAKE algorithm[93], the bond length and bond angle between oxygen and hydrogen atoms assigned as 0.1 nm and 109.47°, respectively. The charge for the oxygen and hydrogen atoms are given as +0.4238e and -0.8476e, respectively.

For the columbic and dispersive interactions between water molecules, a distance cut of chosen to be 1 nm. Besides, a particle-particle-particle (PPPM) mesh solver is used to assess the long-range Coulombic forces. Intermolecular interactions between the atomic pairs are described by using Lennard-Jones (LJ) and Coulombic potentials are given as,

$$\Phi(r_{ij}) = 4\varepsilon_{ij}\left(\left(\frac{\sigma_{ij}}{r_{ij}}\right)^{12} - \left(\frac{\sigma_{ij}}{r_{ij}}\right)^{6}\right) + \frac{1}{4\pi\varepsilon_0}\sum_{i}^{a}\sum_{j}^{b}\frac{q_i q_j}{r_{ij}} \tag{1.16}$$

where ε, ε_0, σ, q_i, and r_{ij} represent well depth, dielectric constant, molecular diameter, particle charges, distance among charged pairs, respectively. The potential parameters for atomic pairs are given in Table 1.1. In general, the L-J potential parameters in the literature are for the same type of atoms. Generally, Lorentz-Berthelot (LB) and similar mean calculation rules are applied when the interaction of different atoms to each other is examined. LB mixing rule given as,

$$\sigma_{Si-O} = \frac{\sigma_{Si-Si} + \sigma_{O-O}}{2}, \quad \varepsilon_{Si-O} = \sqrt{\varepsilon_{Si-Si} \times \varepsilon_{O-O}} \tag{1.17}$$

However, these simple average calculations cannot predict actual surface interactions. The interaction strengths between different materials are still a growing subject in MD. At this stage, instead of the LB rule, parameters that proved correct in the earlier study[94] were used to model the interactions among silicon and oxygen atoms. The strength value for silicon-oxygen interaction (ε=0.01511 eV) that was determined to restore the experimentally tested hydrophobic behavior of silicon surfaces. The Large-Scale Atomic/Molecular Massively Parallel Simulator (LAMMPS) Code[95] is performed in this research.

Table 1.1. The parameters for molecular interaction of atomic pairs

Atomic pair	σ (Å)	ε (eV)	q (e)
H-H	0	0	0.4238
O-O	3.166	0.006739	-0.8476
Si-O	2.633	0.01511	0

CHAPTER 2

WETTING OF NANOPATTERNED SILICA SURFACES

2.1. Simulations Details

Nanoscale wetting produces size-dependent actions at the three-phase line and at the liquid-vapor interface, and these actions create the line tension effect and Tolman length. To order to determine the pinning effects only, we want to exclude these results. To be able to overcome these effects, we held the water droplet sizes much greater than the Tolman length values (~0.05nm)[96,97] and we produced hemi-cylindrical water droplets to remove curvature-related line tension effects.

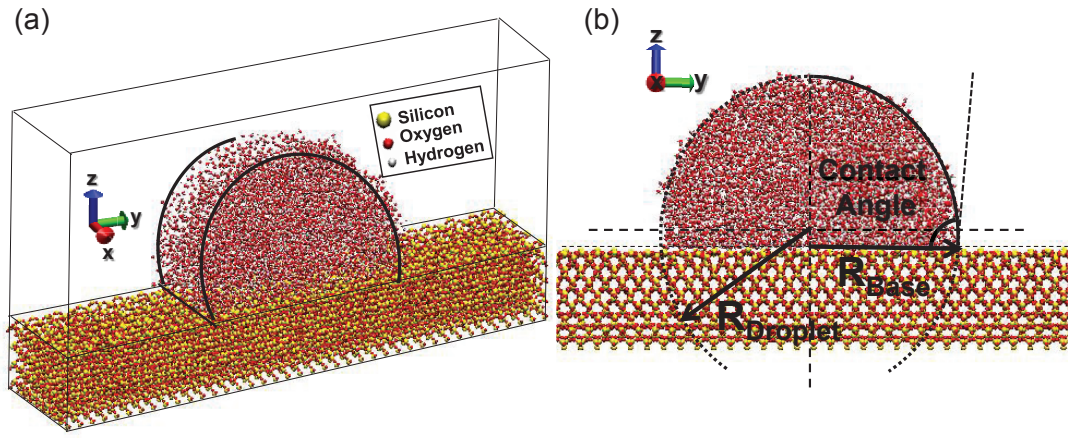

Figure 2.1. (a) The simulation domain of a hemi-cylindrical droplet on a flat silica surface. Atoms shown as yellow, red, and white are silicon, oxygen, and hydrogen atoms, respectively. (b) The contact angle of the snapshot.

The snapshot of a simulation domain for wetting investigations is shown in Figure 2.1. A silica slab and a nano-sized water droplet is used to create the simulation region. Silicon, oxygen, and hydrogen atoms are represented by yellow, red, and white atoms, respectively. On the x and y directions, a periodic boundary condition was applied, while z direction was fixed. As shown in Figure 2.1(a), hemi-cylindrical water droplets have effectively produced on chosen single crystalline surfaces. Also, as seen in Figure 2.1(b)

that the radius of the circle was defined as $R_{Droplet}$, while R_{Base} was defined as where the water droplet touches the solid substrate.

The atom locations were determined with the Verlet algorithm. Furthermore, time step of the simulation is assigned as 0.001ps. The system temperature was raised to 300K using an NVT ensemble and a Nosé-Hoover thermostat. To achieve an isothermal steady state, simulations were run with a 2×10^6 (2ns) time steps. Following that, the NVE ensemble is utilized to accomplish an average of the required properties over 6×10^6 time steps (6ns). At 5ps intervals, the measurement is taken. Elongated rectangular prisms of $\infty \times 0.1\text{nm} \times 0.1\text{nm}$ are employed to dissolve the droplets in the x, y, and z directions, according to the hemi-cylindrical shape of the droplets. In the xz plane, rectangular prism shape bins were used to measure water density. Bin-wise water produced two-dimensional (2D) density contours describing equally dense areas. These average density contours were used to calculate the contact angles.

2.2. Results and Discussion

In traditional theory, compared to the macroscale droplets, how to analyze the wetting of small droplets of nanosized is limited. Precise determination of contact angle for nano sized sessile droplets, additional effects should be considered.

To overcome these effects, the line tension and pinning effect must be detected accurately. Therefore, in MD simulations for this study, hemi-cylindrical droplets are modelled instead of the hemi-spherical ones due to its ability to distinguishing the effect of line tension. Also, to overcome the Tolman length, we created the water droplet sizes much greater than the Tolman length values. However, in order to eliminate the pinning effect, it is necessary to calculate the force that created this effect correctly. These calculations should be made for each nano-patterned surface. In this study[98] we found that the pinning effect on nanopatterned surfaces affects wetting behavior and gives false contact angle results.

The silica slab is modeled as β-cristobalite form due to its similarity of density with the amorphous silica. Also, this form of silica has other advantages because of its crystal structure. In a self-repeating honeycomb structure, crystalline structures in a row can be removed to achieve a pattern sequence. Thus, the nano-patterned β-cristobalite is obtained in 2D domain. We systematically created six different surface structures by

removing the number of silica molecules in the x-, y-and z-direction. The created surfaces are defined as R_{xyz}, where x is the amount of unit roughness elements on the structured pattern, y is the amount of removed unit asperity elements, and z is the number of vertically removed Oxygen-Silicon-Oxygen layers. One-unit roughness element and vertical layer are removed from the surface that surface named as R_{111}. If two-unit roughness element and one vertical layer are removed from the surface that surface named as R_{221}. All the nano-patterned silica surfaces are shown in Figure 2.2.

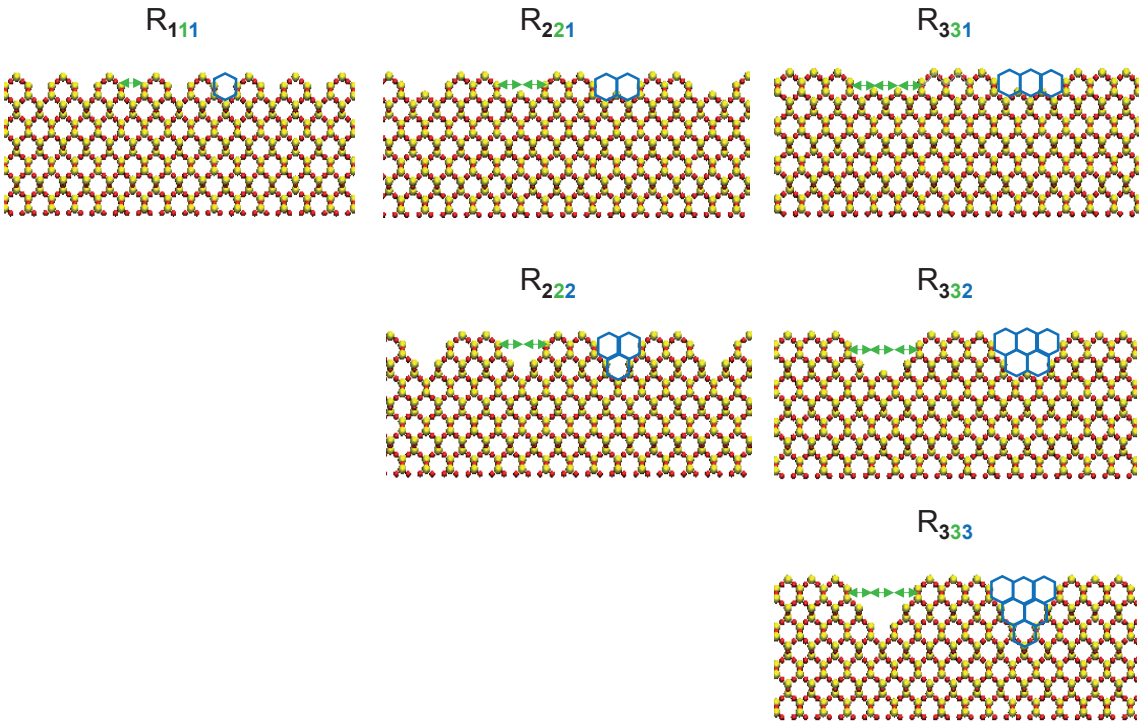

Figure 2.2. Different size nano-patterned silica surfaces.

Different contact angle values were measured at different amounts of water along the same surface structure. Due to the pinning effect, it attaches droplet to the surface structures, increasing the visible contact angle. Density contours of the R_{111} case for three different base sizes are given in Figure 2.3. In this case, droplets are sitting on many different surface patterns, starting from 2 up to 14 patterns. The measured lowest contact angle values are close to the smooth surface value of 95°. While the droplet size grows, the measured contact angle values are increases, but the maximum contact angles of microscopic results decrease.

The contours of the water droplets on the R_{221} and R_{222} surfaces are shown in Figure 2.4. In these cases, the maximum surface pattern coverage drops to 5 for R_{221} and 6 for R_{222}. As a result, the contact angles measured at R_{221} and R_{222} are larger than those

measured at R_{111}. The minimum contact angle values are around the flat surface. However, maximum angle values are quite large compared to the flat surface result.

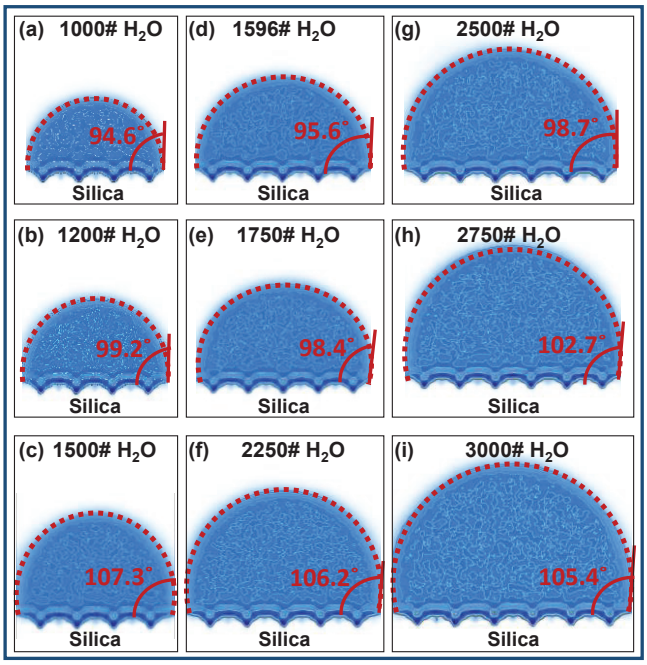

Figure 2.3. Density contours and related contact angles of the R_{111} surface for various droplet sizes.

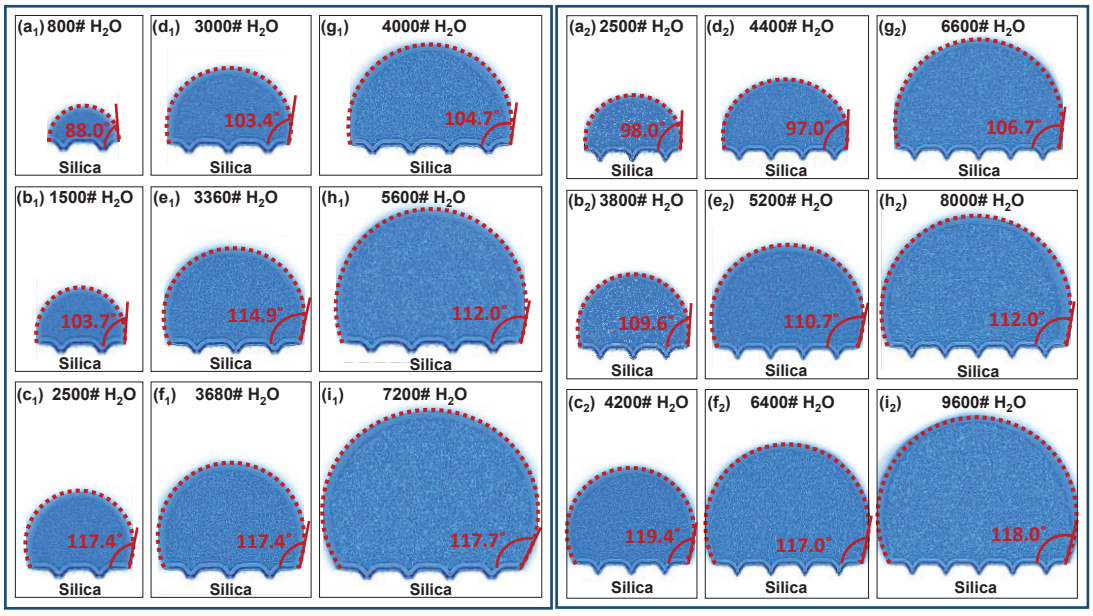

Figure 2.4. Density contours and related contact angles of the (1) R_{221} and (2) R_{222} surfaces for various droplet sizes.

In Figure 2.5, the density contours of the R_{331}, R_{332} and R_{333} surfaces can be seen. In these cases, pattern coverage reduces more, the computational limit was achieved with 15000 water molecules for the droplet with the R_{333} surface pattern. As a result, we might only be able to replicate four microscopic states for R_{331} case, three for R_{332} case, and two for R_{333} case. Despite the fact that the minimum contact angles are oriented around the flat surface, maybe even a little higher, the maximum contact angles are relatively large compared to the flat surface result.

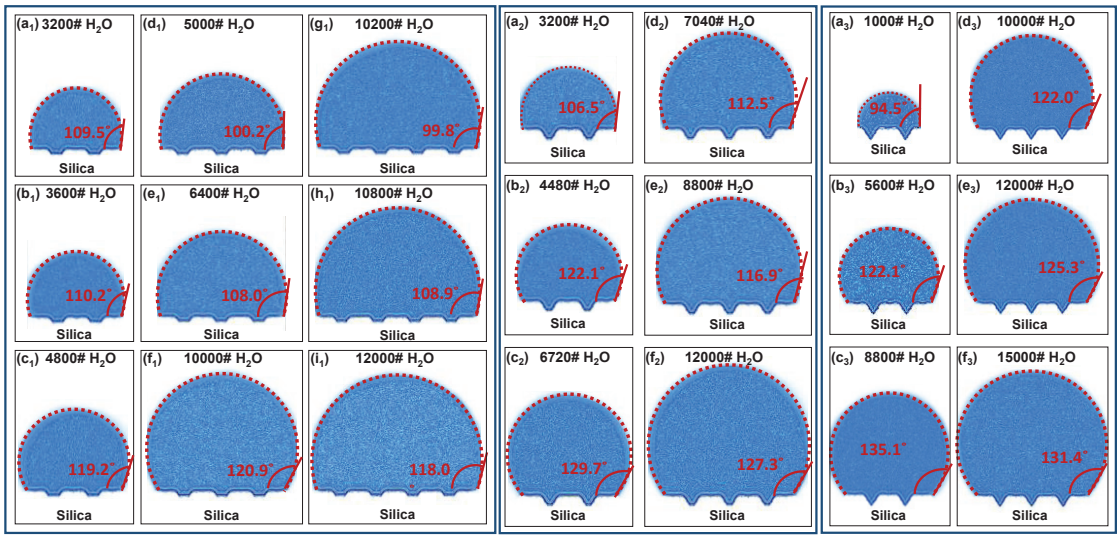

Figure 2.5. Density contours and related contact angles of the (1) R_{331}, (2) R_{332} and (3) R_{333} surfaces for various droplet sizes.

In order to get rid of pinning effect, the linear change of the contact angle for 6 different surface types (R_{111}, R_{221}, R_{222}, R_{331}, R_{332} and R_{333}) is considered. The change of the contact angle with different surface structures with different droplet volumes is shown in Figure 2.6. As droplet radius increases the number of patterns that droplet sits increases. For adding more water molecule to the system, the behavior, the pinning characterization is made. When the droplet is pinned at the edges and it stays on the same number of patterns during increasing droplet size, we observed that the contact angle changes linearly. In order to characterize pinning effect and evaluate the correct contact angle for each heterogeneous surface, the droplet size is normalized with the covered pattern size ($R_{D\text{-}FS}$/P). For the droplet size, free-standing cylindrical droplet radius ($R_{D\text{-}FS}$) is used, and it is only function of the droplet volume. In this research, we are showed the results for the force acting on the pin and we are characterized the pinning effect for 6 different surface types[98]. Also, with eliminating the pinning effect, we are established the

equilibrium contact angle results for 6 surface types R_{111}, R_{221}, R_{222}, R_{331}, R_{332}, and R_{333}. As a continuation of this results, we are estimated the macroscopic contact angles for all surface types. The contact angles of various sized droplets on numerous surface heterogeneities are given in Figure 2.7 for 6 surface types (R_{111}, R_{221}, R_{222}, R_{331}, R_{332}, R_{333}). Finally, macroscopic behavior of the droplets is examined, and we estimated the equilibrium contact angle of the appropriate nanopatterned surface excluding the pinning effects. With a constant pinning effect, the contact angle is found to be proportional to droplet radius. In Figure 2.7, linear approximations are used to calculate the minimum and maximum angle change of each microscopic group. The microscopic behavior of different patterns is constrained by the dotted dashed lines, which determines the linear microscopic change of contact angles with a reducing slope. The projections of the dotted dashed lines converge at the equilibrium contact angle of the different surfaces. Equilibrium contact angle results are shown in Table 2.1 for each surface. It was discovered that when surface heterogeneity increased, the equilibrium contact angle increased as well. The contact angle increases from 95° to 106°, 111°, 115°, 119°, 122°, and 125° with increasing surface structure size.

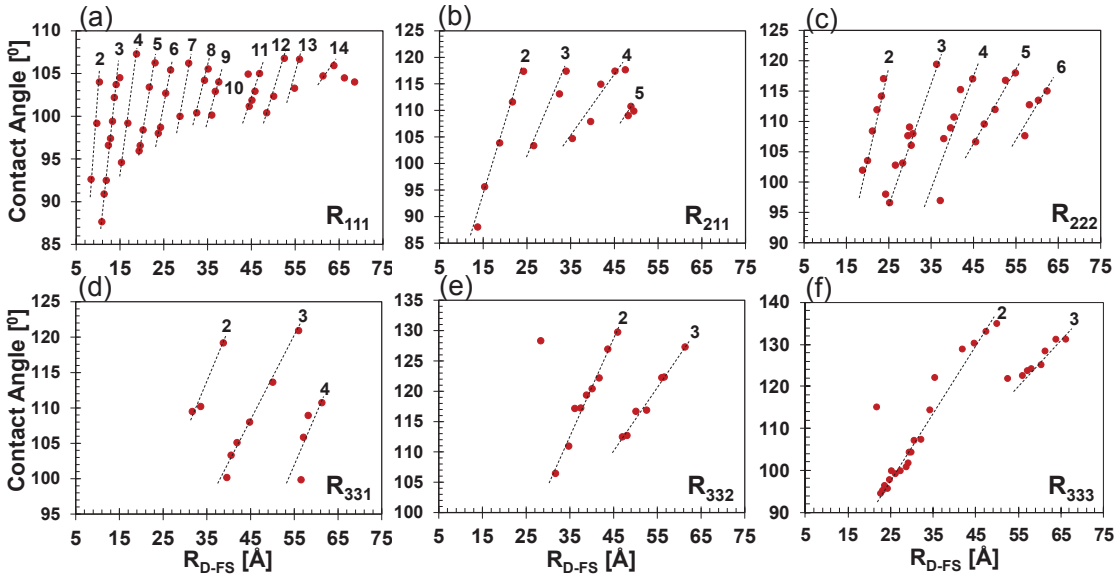

Figure 2.6. The contact angle change with the volume of the droplet on the different surface structures. (a) is the smooth surface, (b) is R_{111} surface, (c) is R_{221} surface, (d) is R_{222} surface, (e) is R_{331} surface, (f) is R_{332} surface, (g) is R_{333} surface. The dashed lines relates contact angle results to the same number of nano-patterns, when the upper insets give the number of patterns that droplet sits.

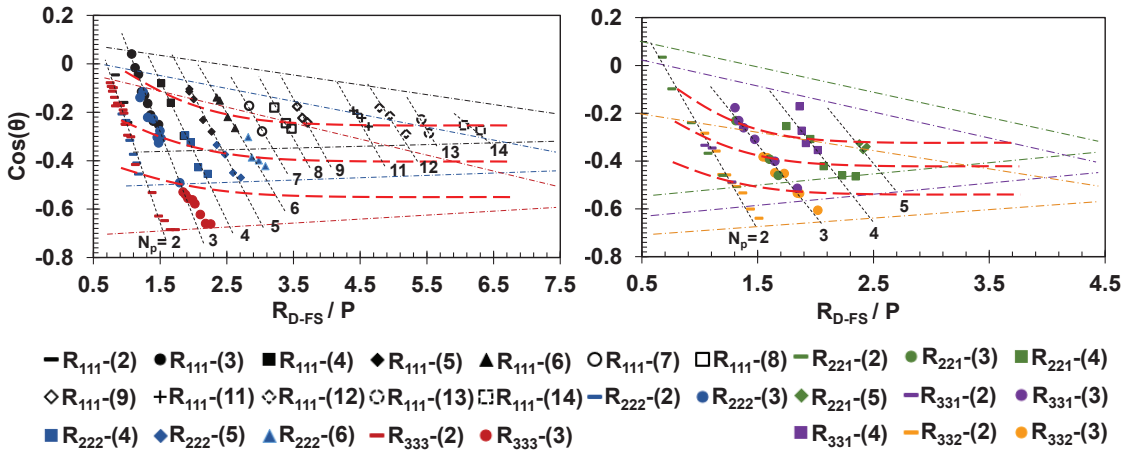

Figure 2.7. Cosine of contact angles of droplets of various sizes with normalized droplet size (R_{D-FS}/P) for surface types of R_{111}, R_{222}, R_{333}, R_{221}, R_{331}, R_{332} The colors represent the size of the surface design, while the symbols show the number of patterns covered. Inverse linear curve fitting approximates the average contact angles of each microscopic groups such as $1/R_{D-FS} \rightarrow 0$.

Table 2.1. The equilibrium contact angle results of all nanostructured surfaces

Smooth	R_{111}	R_{221}	R_{222}	R_{331}	R_{332}	R_{333}
95.0°	106.0°	111.0°	115.0°	119.0°	122.0°	125.0°

Next, it was desired to understand whether the pinning effects have an inverse linear dependence. Consequently, an inverse linear fit was used in Figure 2.7 to determine the pinning effects on macroscopic behavior using the contact angles of each microscopic group. At the $1/R_{D-FS} \rightarrow 0$ limit, linear predictions are used for the equilibrium contact angle. Figure 2.7 also displays the inverse linear relation between pinning and droplet size, which is not adequately representative of the overall macroscopic behavior, although it achieves the same equilibrium contact angle at the negligible pinning limit. An important result of this study was that when the diameter of the free-standing droplet is about equivalent to 24 times the size of the surface structure, the pinning effect vanishes.

Contact angle measurements were also desired to be made within other solid/liquid surface interaction values. However, in cases of $\varepsilon = 0.1$ and $\varepsilon = 0.01$, the droplet did not stay on the surface, and the equilibrium contact angle values of the surface could not be achieved, as the surface became superhydrophobic. Each measurement could

be done at different time steps, then the average of the results can be obtained for these surfaces.

2.3. Conclusion

In this study, wetting on nano-patterned silica surfaces was investigated by MD to understand the pinning effect. As a result, it was found that the pinning effect on nano-patterned surfaces affects the wetting behavior. The contact angle of nano-patterned surfaces varies depending on the droplet volume. The wetting angle increases with increasing droplet volume related to the pinning effect, and it continues to increase until it surpasses the pinning force it is subjected to. After this pinning effect yields, it moves to the next heterogeneous surface and repeats the same process. The pinning effect was found to be directly associated to free-standing droplet radius ($R_{D\text{-}FS}$). When this individual droplet radius was normalized with the matching surface pattern size ($R_{D\text{-}FS}/P$), a correlation was found between the wetting behavior of various sized droplets. In this context, pinning effects were conducted as a function of $R_{D\text{-}FS}/P$, which is free from droplet size and surface roughness. As the droplet size increases, the pinning effect decreases and becomes insignificant, and the contact angle approaches the equilibrium value. It was detected that the equilibrium contact angle increases as the surface heterogeneity increases. With increasing surface structure size, the wetting angle of the surfaces increase from 95° to 106°, 111°, 115°, 119°, 122° and 125°. The size limitation of pinning effect is one of the most important implications here. As the droplet volume increases, the maximum and minimum contact angles of each microscopic group converge. Thus, the difference between advancing and receding angles decreases with increasing droplet volume. As a final and essential conclusion of this research, the pinning effect vanishes when the diameter of the free-standing droplet is equal to 24 times the size of the surface structures.

CHAPTER 3

FLUID TRANSPORT ON NANOPATTERNED SILICA SURFACES

3.1. Simulations Details

In the second part of the thesis, we wanted to investigate the fluid transport of nanopatterned silica surfaces. Molecular dynamic simulations are conducted on a 3-D model of liquid water molecules enclosed within solid silica walls, as shown in Figure 3.1.

.

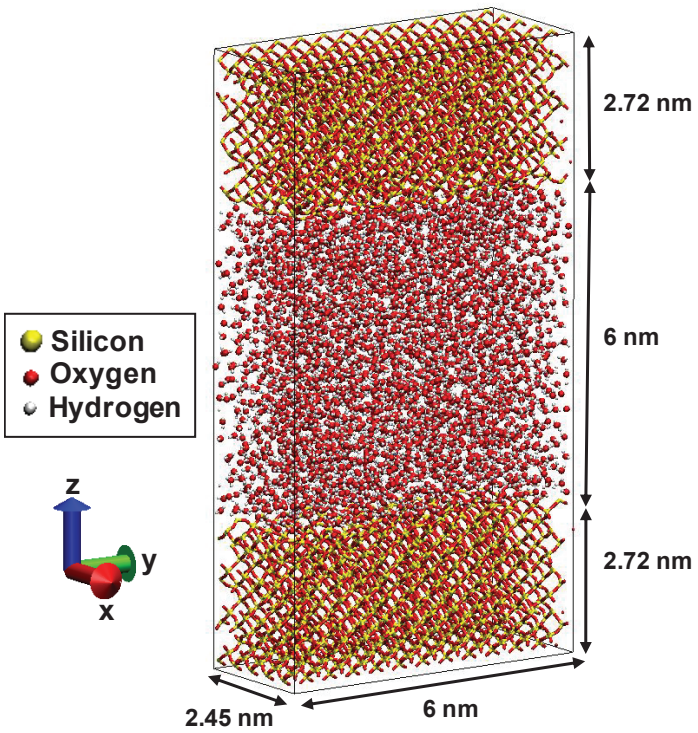

Figure 3.1. Three dimensional schematic illustration of the simulation domain for silica nanochannel water transport. Silicon atoms represented by yellow atoms. Oxygen, and hydrogen atoms are represented by red, and white atoms, respectively.

The dimensions for the simulations assigned as 2.45nm in the x-direction, 6nm in the y-direction, and 11.44nm in the z-direction. In both the x and y directions, the simulation box has periodic boundary conditions. The channel height (h) has been assigned as 6 nm.

The continuum fluid mechanics assumptions are applied for flow transport systems. The Navier-Stokes equation can be simplified for force-driven Newtonian fluid flows for steady, incompressible, fully developed flows as

$$\frac{d^2u}{dy^2} = -\frac{f}{\mu} \tag{5.1}$$

where μ, f, and $u(z)$ are the viscosity, driving body force, and the velocity field, respectively. In nanochannels, the creation of the force-driven water flow between silica surfaces cause slip behavior due to its size effects. The slip length may vary with the different surface patterns.

We are obtained the velocity profile for slip flow with deriving the Navier-Stokes equations. With applying the boundary conditions ($y = 0$ and $y = h$) to each wall by using the constant slip length L_s on both surfaces. The velocity profile can be obtained as

$$u(y) = \frac{fh^2}{2\mu}\left(-\left(\frac{y}{h}\right)^2 + \left(\frac{y}{h}\right) + \left(\frac{L_s}{h}\right)\right) \tag{5.2}$$

Polynomial curve fitting approach was used to calculate the slip lengths from the MD results[10,99,100]. The form of parabolic velocity profile $u(y) = Ay^2 + By + C$ is matched to the MD simulation results and related with Eqn. (5.2). Hence, the slip length is calculated by using equation below

$$L_s = \frac{2\mu C}{fh} \tag{5.3}$$

This part of the research, the well-known flow model of Poiseuille flow is designed between two walls with the patterned structures to determine the slip behavior.

Each system is balanced thermally by using the NVT ensemble. The thermodynamic condition of the water was determined by keeping the temperature 300K using the Nose-Hoover thermostat and the density of the water is maintained around 993.7 kg/m3 for each case.

In-channel flow simulations were carried out across 7 different surface types as shown in Figure 3.2. The designed channel pattern structures. (a) is the smooth surface, (b) is R_{111} surface, (c) is R_{221} surface, (d) is R_{222} surface, (e) is R_{331} surface, (f) is R_{332} surface, (g) is R_{333} surface. When creating flow simulations, the flow rate in the channel is adjusted to be 40-60 m/s. Therefore, the amount of force applied to the molecules has been adjusted for each case. Flow movements are examined with each created surface, and when the surface structures are changed, the variations in the flow are measured. The nano-size molecular details formed due to the surface structures have been carefully applied to the calculations in the density, momentum exchange and pressure definition.

3.2. Results and Discussion

In this section, in order to observe the surface pattern effect, we are created seven different surface structures and observed the slip behavior of each designed channels as shown in Figure 3.2. In Figure 3.2(a), the nonstructural (smooth) version of the β-cristobalite silica surface is given. Patterns are created in the form of honeycomb structure. The unit roughness element is assumed to be a repeating honeycomb structure. R_{xyz} represents the unit roughness elements amount on the nanopattern, y represents the amount of removed unit roughness elements, and z represents the number of O-Si-O layers vertically removed from the surface. In addition, one-unit roughness element and vertical layer are removed from the surface that surface named as R_{111} which is given in Figure 3.2(b). If the one-unit roughness element and two vertical layers are removed from the surface that surface named as R_{221} which is given in Figure 3.2(c). If the two-unit roughness elements and two vertical layers are removed from the surface that surface named as R_{222} which is given in Figure 3.2(d) If the three-unit roughness elements and one vertical layer are removed from the surface that surface named as R_{331} which is given in Figure 3.2(e). If the three-unit roughness elements and two vertical layers are removed from the surface that surface named as R_{332} which is given in Figure 3.2(f). Correspondingly, the three-unit roughness elements and three vertical layers are removed

from the surface that surface named as R_{333} which is given in Figure 3.2(g). For each case, with applying the atomic forces we are created a flow in y-direction along channels. We are created the well-known flow model of Poiseuille flow between two parallel plates with patterned surfaces. The NVT ensemble is applied to system to kept the system at T=300 K. For all seven cases the density kept around 993.7 kg/m^3.

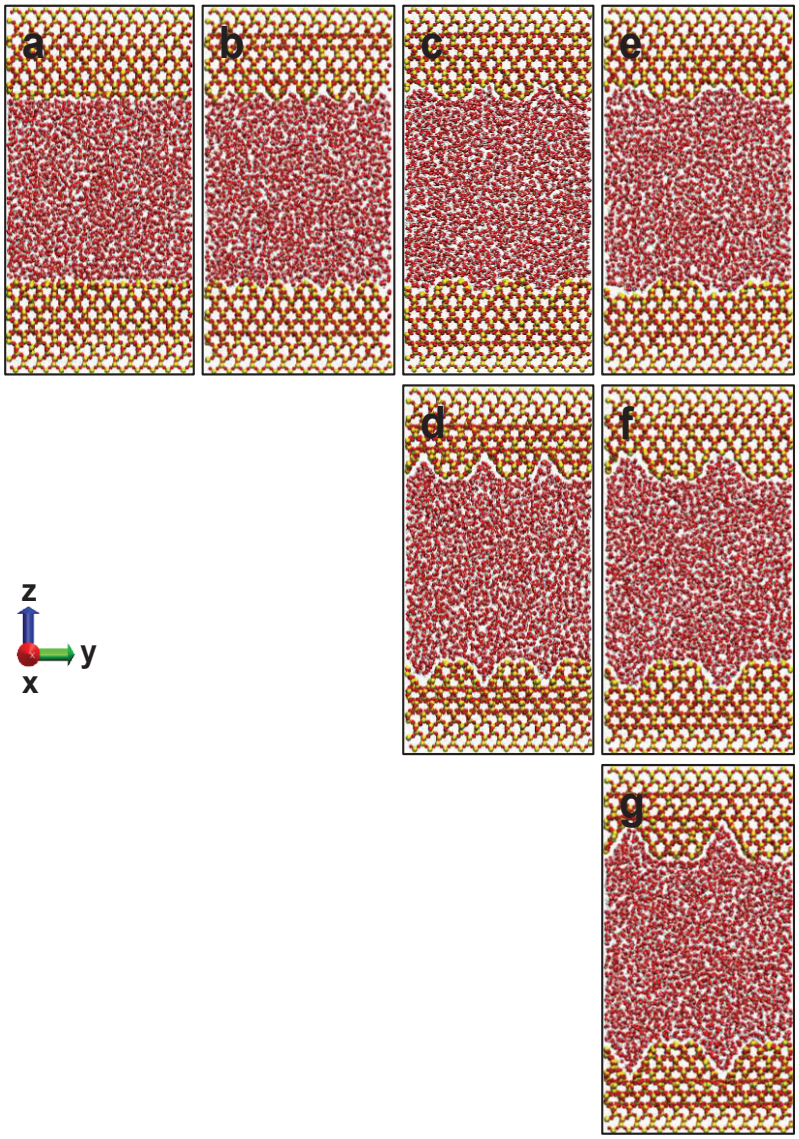

Figure 3.2. The designed channel pattern structures. (a) is the smooth surface, (b) is R_{111} surface, (c) is R_{221} surface, (d) is R_{222} surface, (e) is R_{331} surface, (f) is R_{332} surface, (g) is R_{333} surface

To learn more about how solids and liquids interact at the interface, 2D density models were examined for each structured surface type as shown in Figure 3.3. After that the velocity profiles and slip lengths of the force-driven flow is established. By determining the exact wall locations along the structured surfaces, the density variations are used as a reference parameter for velocity profiles.

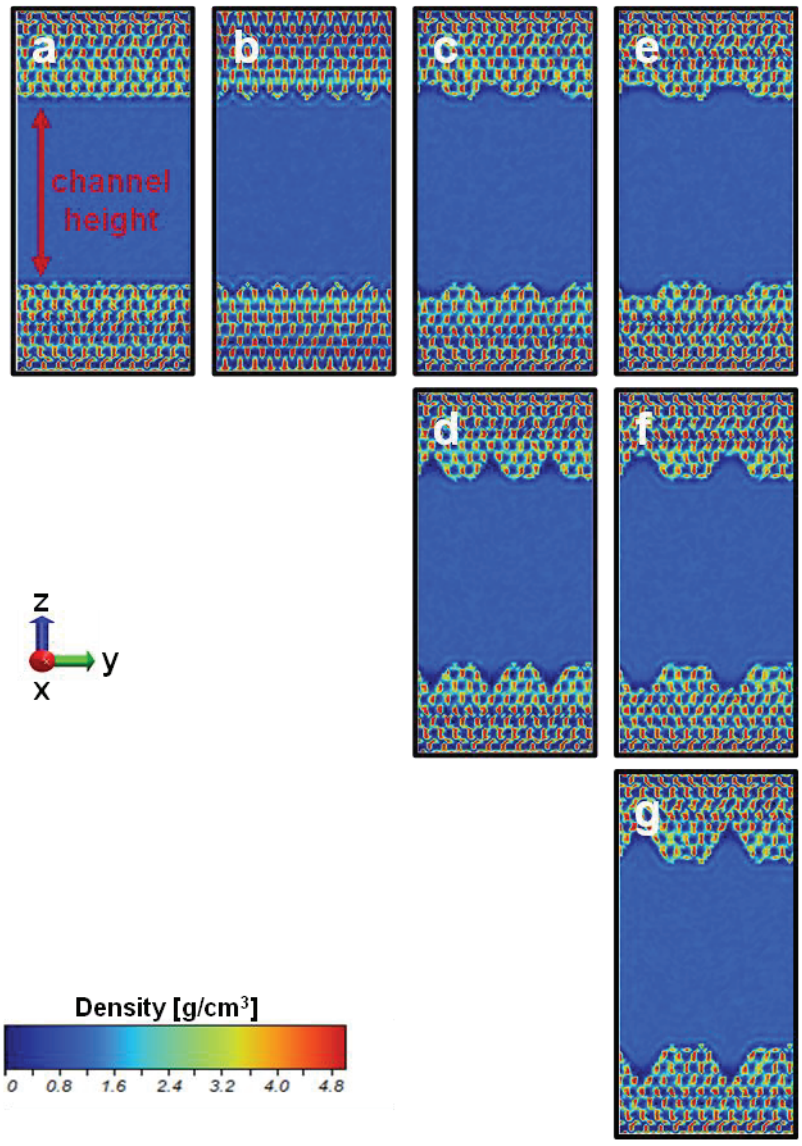

Figure 3.3. Density contours of the designed channel structures. (a) is the smooth surface, (b) is R_{111} surface, (c) is R_{221} surface, (d) is R_{222} surface, (e) is R_{331} surface, (f) is R_{332} surface, (g) is R_{333} surface.

Due to the fact that water molecules unable to approach to solid walls more than their diameter the density pick points near the wall assumed as the wall locations for the structured surfaces by determining the slip lengths of the surfaces. The channel height measured from these points was established as 5.40 nm instead of 6 nm originally determined. There is a narrowing of two water molecule diameter ($\sigma \sim 0.30$) in the channel. The pick points can be identified in Figure 3.3, as the light color blue line near the walls. The region between the density pick points and the appearance of wall is considered unstable for the slip length measurements.

The local slip length measurements are done with two structured cases as can be seen Figure 3.4(c) and (d). These cases have been chosen as the lowest and the highest roughness level, and the velocity profiles of these cases can be seen in Figure 3.4(a) and (b). The measurements were made primarily along the channel structure and shown as local points. Then, as can be understood from velocity profiles, measurements were made based on top (T) and bottom (B) points and shown as average points in Figure 3.4(c) and Figure 3.4(d). Additionally, local and average slip lengths are in compatibility. It has been conducted that the slip length (L_s) varies across the channel along the top and bottom regions along each rough surface, and the slip length (L_s) differs in the top and bottom sections. Figure 3.4(c) shows the Ls values calculated for R_{111} surface type and the locations where these values are measured along the channel. It is seen that Ls value systematically decreases in the bottom regions. The reason for this reduction is thought to be the decrease of the velocity of the water molecules filling the cavities towards the bottom. To understand the change of L_s values along the top and bottom parts, the variation of each velocity profile along the channel was shown in Figure 3.4(a) and Figure 3.4(b). As seen in Figure 3.4(d) which is the R_{333} case where the cavity size at its maximum, Ls values decrease gradually. The R_{333} cavity structure is deeper than the R_{111} structure and will be seen as it descends to the bottom of the cavity that Ls values have decreased considerably. However, the average L_s values calculated in the cavities are very close to each other in both surface types. The average L_s values calculated for each surface type coincide with the slip length values calculated in the top regions. Top values are taken as the L_s values determined for each surface structure.

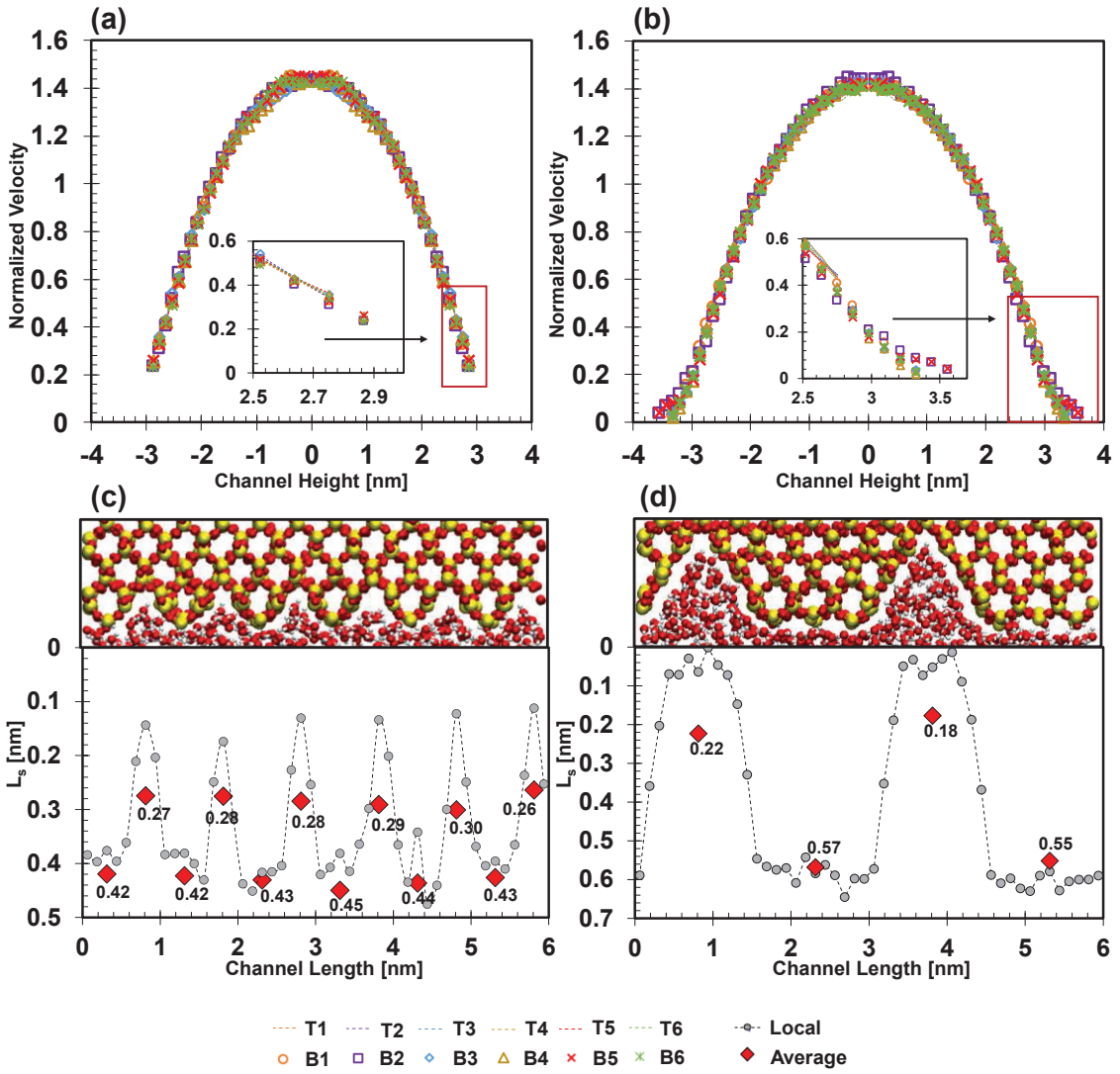

Figure 3.4. The local velocity profiles of the two different roughness structure. T represents the top part of the roughness and B represents the bottom part. (a), (c) are the velocity profiles, local and average slip length results of R_{111} case and (b), (d) are the velocity profiles, local and average slip length results of R_{333} case.

Channel velocity profiles of each surface type obtained as a result of simulations are given in Figure 3.5. Since, it is known that liquid/solid interaction energies have a direct influence on the slip velocity along each rough surface type, in order to examine this effect in detail, liquid/solid interaction energies ε_{wf} for both ε_{Si-O} and ε_{O-Os} was reduced by 10 times and 100 times for each rough surface type, and the influence of this interaction on slip length (L_s) was investigated. The amount of force applied has been adjusted so that the flow velocity remained within the channel as 40-60 m/s.

According to the results, the effect of nanopatterning on the slip behavior was examined and the effect of this behavior on the wetting angle was also conducted. Based on the literature information collected in previous studies, we wanted to obtain a relation between slip length and contact angle with the proposed theories. We wanted to see how well these theories fit with our results. With eliminating the pinning effect, the correct contact angle values for the heterogeneous surfaces were found. For the contact angle results, determined equilibrium contact angle values are used. We computed slip and contact angle results then applied the models suggested by two basic studies on the data we obtained. The theory[41] that created by Huang et al. as denoted in Eqn. (1.6) is found to be consistent for our cases. Eqn. (1.6) which is $L_s \sim (1+\cos\theta)^{-2}$, is suggested that the slip length (L_s) is related with the solid/liquid friction coefficient λ and shear viscosity η as $L_s = \eta / \lambda$.

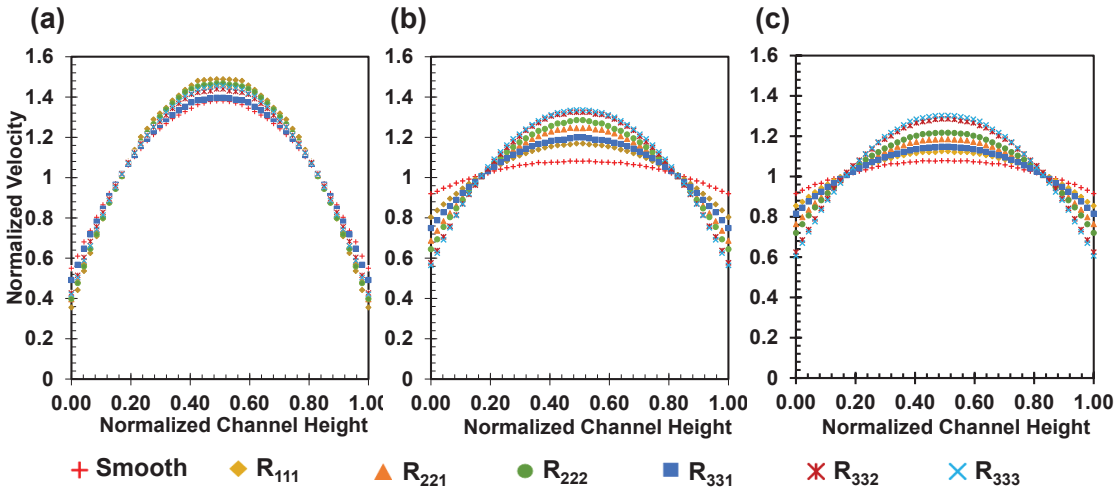

Figure 3.5. The velocity profiles of each surface type. (a) is the ε=1.0 case, (b) is the ε=0.1 case, (c) is the ε=0.01 case

For the flat (smooth) surface slip length and contact angle measurements, the liquid/solid interaction energies ε_{wf} for both ε_{Si-O} and ε_{O-Os} was reduced by 0.05 times. By reducing the wall-fluid interaction energies gradually, 10 different slip length and contact angle values are obtained. Figure 3.6 depicts the findings for the flat surface. Although our structured surface results are close to the theory of Huang et al., A one-to-one agreement was observed only for the flat surface. For this reason, the roughness on the surface increases, the friction increases, so the slip length decreases. However, we

saw that with increasing roughness, the relation moves further away from the theory. For all surfaces in this study, Figure 3.7. shows slip length as function of contact angle.

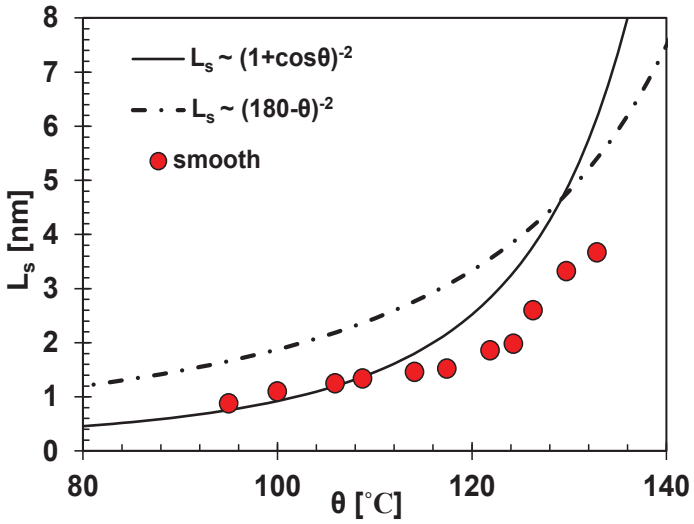

Figure 3.6. Relationship between $L_s \sim (1+\cos\theta)^{-2}$ theory (straight line) presented by Huang et al., $L_s \sim (180^\circ-\theta)^{-2}$ theory (dashed line) presented by Sender et al. The values represents the flat surface results.

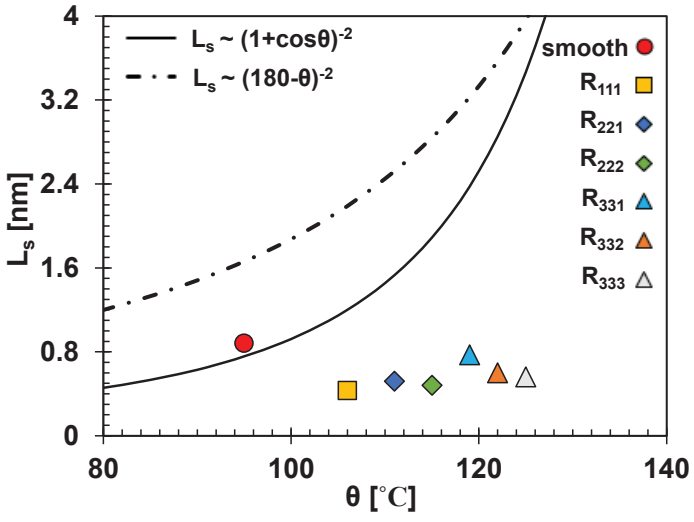

Figure 3.7. Relationship between $L_s \sim (1+\cos\theta)^{-2}$ theory (straight line) presented by Huang et al., $L_s \sim (180^\circ-\theta)^{-2}$ theory (dashed line) presented by Sender et al., and slip length (L_s) and wetting angle values. Colors and shapes show different types of surfaces.

3.3. Conclusion

In this study, force-driven water flow through surface patterned silica nanochannels is evaluated using molecular dynamic simulations. Then, the slip behavior of water transport in silica nanochannels with a limited channel length is estimated for the designed surface patterns. By systematically changing the surface nanostructures, the impacts of surface roughness on slip behavior are investigated. We showed that the nano-sized surface structures formed on the surface change the slip behavior, and we determined the relation of the surface patterning with the slip length. The solid-liquid interactions that determine the velocity slip can also resolve the surface wetting dynamics. Therefore, the velocity slip and the resulting fluid transport can be predicted and controlled by wetting dynamics or contact angles.

For this reason, we examined the flow behavior in seven different surface structures and three different solid/liquid interaction parameters and calculated the slip lengths of these flows. A relationship was established between the calculated slip lengths and the surface roughness. As a result, it was found that the slip length decreased as the surface roughness increased. Additionally, we compared the slip behavior for different designed surface structures with the contact angles measured on these structured surfaces using proposed theories. Then, the models suggested by the previous two main studies were applied on the data we obtained. We found that our results are more consistent with the presented theory of $L_s \sim (1+\cos\theta)^{-2}$. Although our results are close to Huang et al, we observed one-to-one compatibility only for the flat surface. We think that this is because as the roughness on the surface increases, the friction increases, and the slip length decreases. We also noticed that the theory is distanced as the amount of roughness on the surface increases.

CHAPTER 4

EVAPORATIVE HEAT TRANSFER AT NANOPATTERNED SILICA SURFACES

4.1. Simulations Details

In the third study of the thesis, the nanoscale droplet evaporation is investigated by using MD simulations with heating the silica surface. The water droplet, vapor, and the silica solid substrate were all present in the systems. Water is used in droplet modeling, and the beta-cristobalite form of silica is used as a solid substrate. As it done before, the SPC/E water model is also used in this study.

The number water molecules chosen to be 2500. The simulation area for evaporation of a nanoscale cylindrical droplet on a silica substrate is shown in Figure 4.1. The x and y directions are subjected to periodic boundary conditions, but the z direction remains fixed.

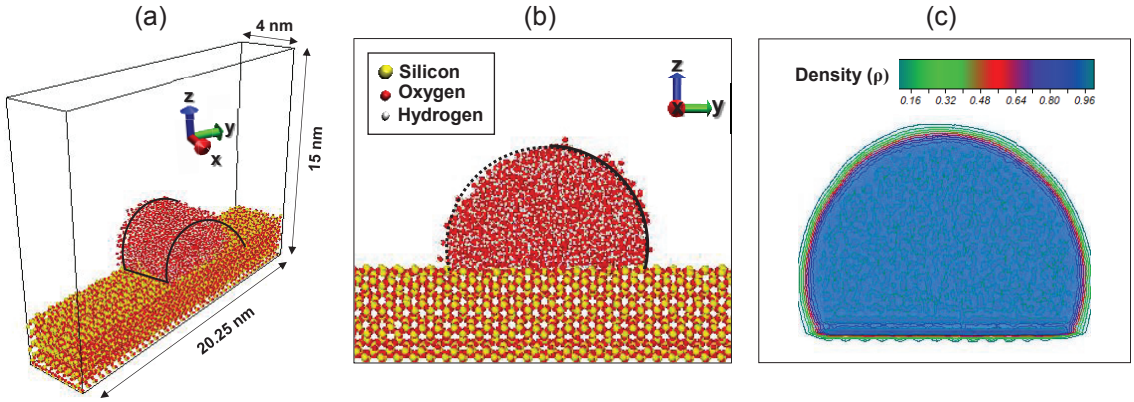

Figure 4.1. (a) The simulation domain of a hemi-cylindrical droplet on a flat silica surface, side view. (b) Schematic illustration of the droplet snapshot from front view. The yellow, red, and white atoms corresponds to silicon, oxygen, and hydrogen atoms, respectively. (c) density contours of the droplet

As seen in Figure 4.1(a), hemi-cylindrical water droplets formed on the crystal surface of the silica. As mentioned earlier, the droplets were modeled as hemi-cylindrical,

eliminating nanoscale wetting effects. The simulation dimensions of x, y, and z were chosen to be 4nm, 20.25nm, and 15nm, respectively. The density contours of the equilibrium droplet are shown in Figure 4.1(c).

The atom locations were calculated as a time step at 0.001ps intervals using the Verlet algorithm. Molecular interactions parameters for atomic pairs are used as they mentioned in Table 3.1. The simulations were carried out using LAMMPS[82].

To generate an isothermal steady state, the temperature is managed with NVT ensemble at 300K with 2×10^6 timestep (2ns). Then, over 2×10^6 timesteps, the microcanonical ensemble (NVE) was utilized to average the required properties (2ns). A vapor phase surrounded each droplet as each system relaxed into its equilibrium form. The simulations were run on smooth (R_0), R_{111}, R_{222}, and R_{333} structured surfaces at a temperature of 300K. The NVT ensemble was utilized in the simulations and the temperature of the silica substrate is then gradually increased from 300K to 800K in 5ns with using Nosé-Hoover thermostat. To simulate the heating process, the thermostat is simply applied to a few layers of the substrate atoms. Currently, droplet is yielding to droplet evaporation.

4.2. Results and Discussion

The evaporation simulations are performed for four different surface structures (R_0, R_{111}, R_{222}, and R_{333}), these surfaces can be seen in Figure 4.2. Each simulation was repeated two times, and the results were obtained as the average of them. The whole evaporation of the droplet on R_0, R_{111}, R_{222}, and R_{333} surfaces is shown in Figure 4.2. In Figure 4.2(a) section, snapshots of droplet evaporation of R_0 case are displayed at different times ((1) t=0, (2) t=1.8ns, (3) t=2ns, (4) t=2.6ns, (5) t=3.18ns). Figure 4.2(b) shows snapshots of droplet evaporation for the R_{111} case at different times throughout the simulation ((1) t=0, (2) t=1.7ns, (3) t=2.2ns, (4) t=2.73ns, (5) t=3.41ns). Additionally, in Figure 4.2(c) and (d) sections, evaporation snapshots at different times R_{222} case; (1) t=0, (2) t=1.9ns, (3) t=2.39ns, (4) t=2.76ns, (5) t=3.2ns and R333 case; (a) t=0, (b) t=1.8ns, (c) t=2.3ns, (d) t=2.61ns, (f) t=3.2ns are shown, respectively. As clearly seen in Figure 4.2, the evaporation processes for different surface structures seem similar to each other.

At equilibrium, the vapor phase surrounds the droplet, and the droplet volume remains constant. Figure 4.1(c) depicts the droplet's density distribution. Density results

indicate that there are significant density variations near the solid-liquid boundary which can be related with the strong liquid/solid interactions near the wall.

It can be observed that following the red area in Figure 4.1(c), the density distribution gets significantly lower. As a consequence, the boundary for the droplet was determined as the location where density of the droplet is half of water (0.5 g/cm3), as shown in Figure 4.1(c), predicated on the notion that the "Gibbs dividing surface" [101] for vapor-liquid interface can be located at the average of the liquid and vapor densities.

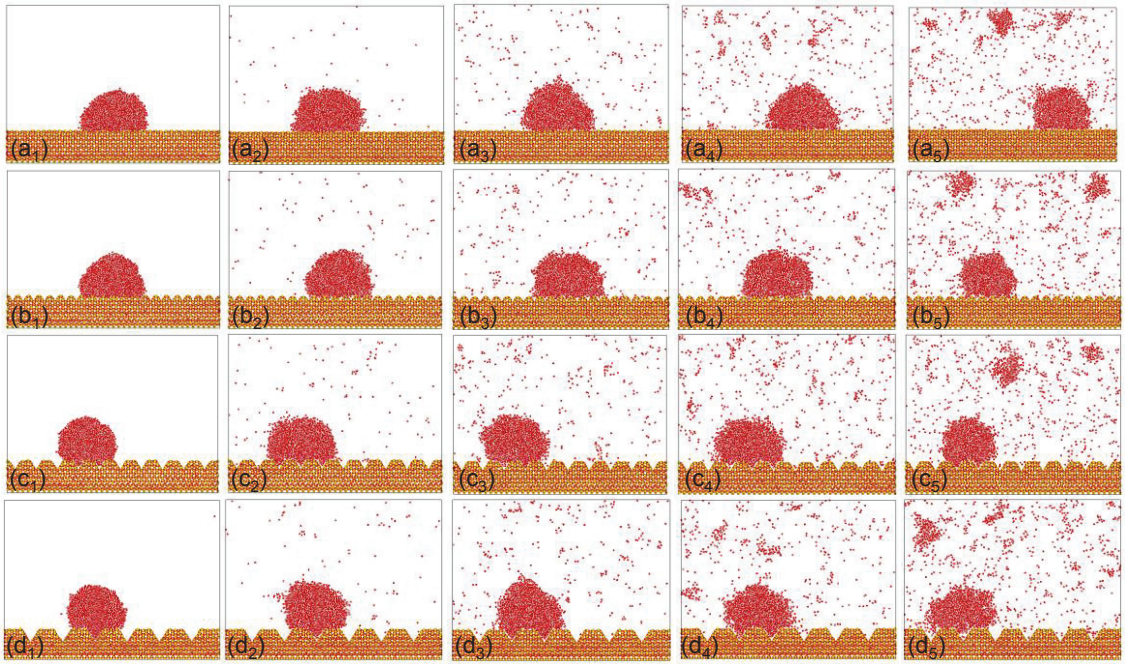

Figure 4.2. (a) Snapshots of the droplet evolution of the R_0 case. (1) t=0, (2) t=1.8ns, (3) t=2ns, (4) t=2.6ns, (5) t=3.18ns. (b) Snapshots of the droplet evolution of the R_{111} case. (1) t=0, (2) t=1.7ns, (3) t=2.2ns, (4) t=2.73ns, (5) t=3.41ns. (c) Snapshots of the droplet evolution of the R_{222} case. (1) t=0, (2) t=1.9ns, (3) t=2.39ns, (4) t=2.76ns, (5) t=3.2ns. (d) Snapshots of the droplet evolution of the R_{333} case. (a) t=0, (b) t=1.8ns, (c) t=2.3ns, (d) t=2.61ns, (f) t=3.2ns

The contact angle distribution for R_{222} case is given in Figure 4.3. As the droplet evaporates over time, the droplet contact angle increases. The contact angle increasing trend with the shrinking droplet of the R_{222} case, and the volume expansion of the droplet appears quite clearly in Figure 4.3. This phenomenon may be related to the formation of bubbles at the solid/liquid interface. Although, the water amount in the droplet decreases

with evaporation, it can be observed that the droplet volume increases, and the droplet levitates away from the surface.

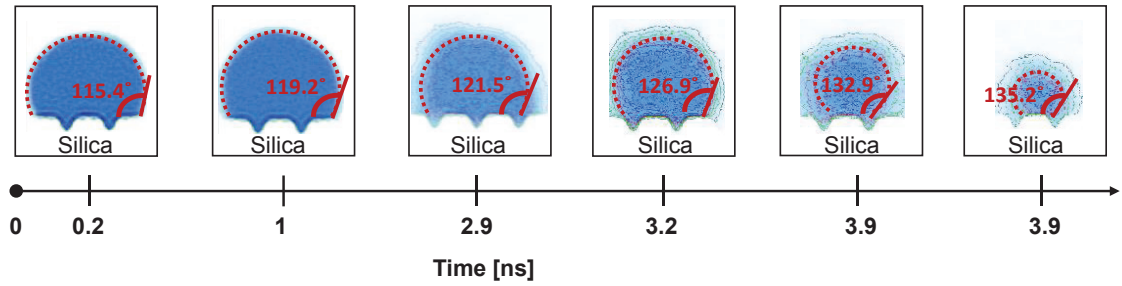

Figure 4.3. The contact angle variation with time for R_{222} case.

The contact angles of the droplets during evaporation are calculated in each period of 100ps, which is seen in Figure 4.4. The contact angle variations are observed during evaporation. The contact angles were measured separately for each surface structures, and it was determined that the contact angles increased throughout the evaporation in each case. The local increases or decreases may be related to the pinning and rapid evaporation kinetics of nanoscale droplets. Also, the Leidenfrost phenomenon can be the reason for the general increasing trend due to vapor layer formation.

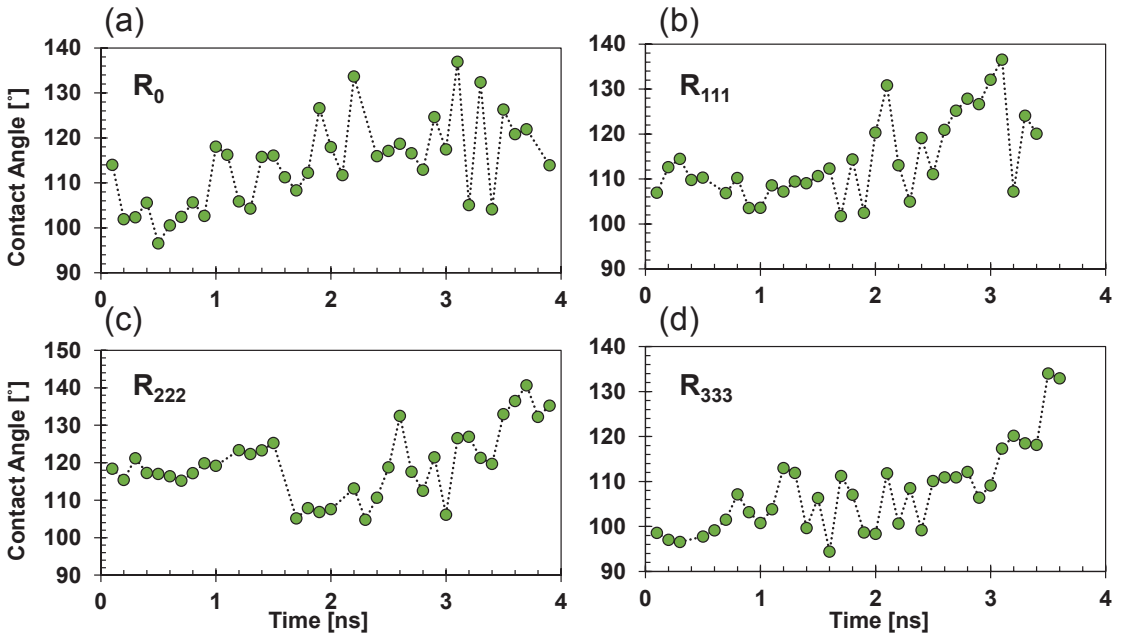

Figure 4.4. The wetting angles of the droplets during evaporation. (a) R_0 surface, (b) R_{111} surface, (c) R_{222} surface, (d) R_{333} surface.

The temperature distribution of the system along the radial direction is calculated to examine the heat transfer as a time dependent property during droplet evaporation. In Figure 4.5, 1-D temperature distribution results are shown in every 0.5ns of the 5 ns total simulation time. Colors, representing each 0.5ns time step, range from black to deep red. Figure 4.5(a), (b), (c), (d) show varying temperature distribution on different surface structures (R_0, R_{111}, R_{222}, and R_{333}), respectively.

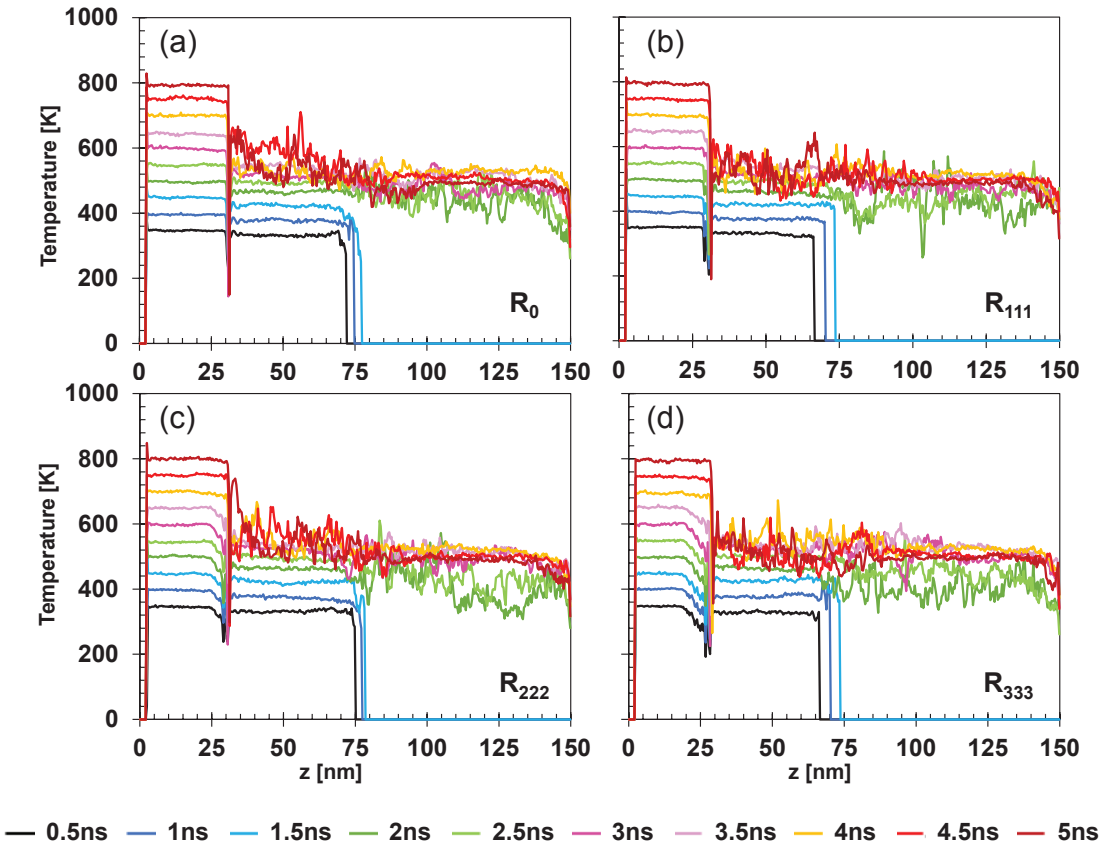

Figure 4.5. One-dimensional temperature distribution in every 0.5 ns of the 5 ns total simulation time. (a) R_0 surface, (b) R_{111} surface, (c) R_{222} surface, (d) R_{333} surface.

Figure 4.5 shows the temperature up to 30nm of the z-direction, the silica temperature is increasing systematically from 300K to target temperature of 800K throughout the simulation. On the other hand, the water temperature increases systematically as silica at first, but the water temperature takes a longer time to increase after 2.5ns of the simulation (After the light green line). After this period, the water temperature begins to remain constant for all the four cases. Therefore, the temperature difference between the solid-liquid phases increases and continues to increase throughout

the evaporation. Transferred heat from silica substrate to water droplet not only increases the temperature but also has a function of water-to-vapor phase change. With 3 ns process time that corresponds to the pink line in Figure 4.5, the water temperature starts to fluctuate since vapor bubbles start to form along the z-direction of the droplet.

The evaporation rate of the droplet is shown in Figure 4.6. The decrease in the number of water molecules was examined at each 100ps time interval. In Figure 4.6(a), (b), (c), (d), droplet evaporation of four different surface structures (R_0, R_{111}, R_{222}, and R_{333}) are examined. Two different cases which are represented by green and yellow circles, have been created for each surface type and the average of these cases has been interpreted.

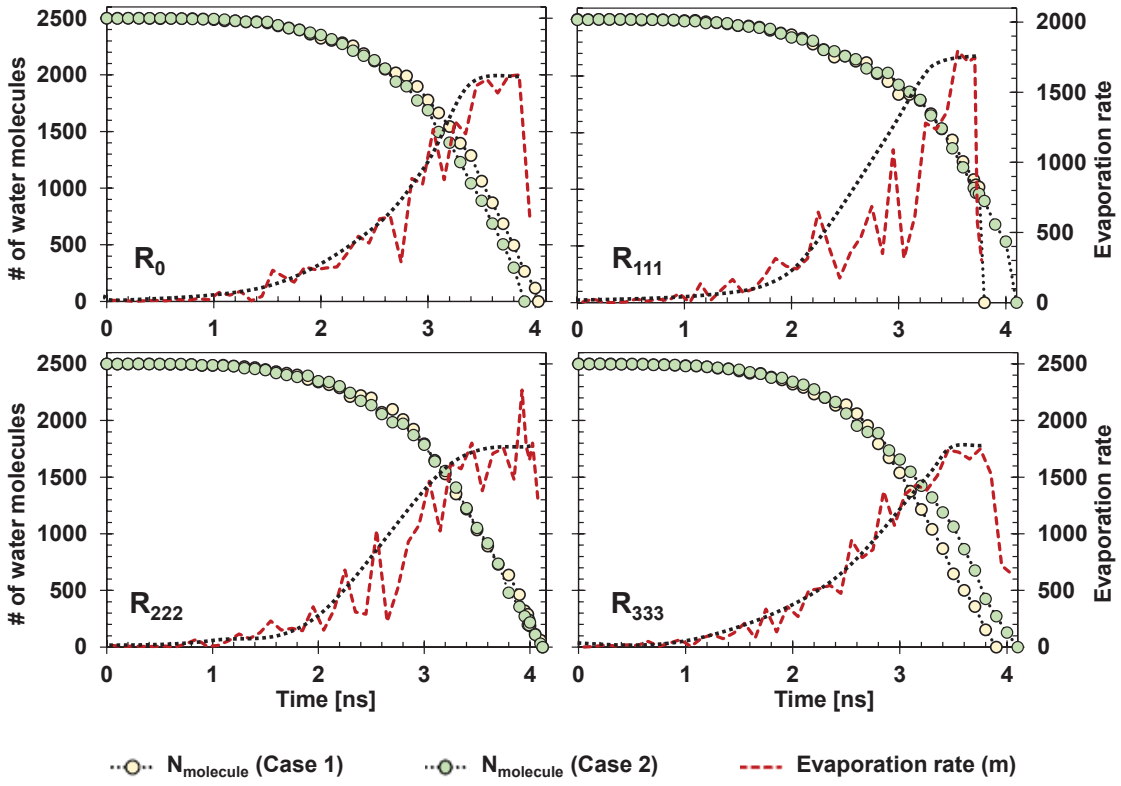

Figure 4.6. Time distribution of droplet evaporation for two different states in two different colors, corresponds to green and yellow circles. The rate of evaporation of the droplet over time, corresponds to the red dashed line. (a) R_0 surface, (b) R_{111} surface, (c) R_{222} surface, (d) R_{333} surface.

Cluster analysis was used to determine the sizes of the droplets and how they changed as they evaporated. If the cutoff distance between two molecules is less than 2.7, they are considered to be part of the same cluster. While characterizing the distance

required for cluster analysis, the free-standing radius of the droplet used in the wetting part was considered. The free-standing radius of each droplet containing 2500 water molecules was calculated as 2.4nm. In addition, an evaporation rate was calculated from this average evaporation distribution and shown in Figure 4.6 with a red dashed line and is calculated as below,

$$m = \frac{\partial N_{molecules}}{\partial t} \tag{4.1}$$

where $N_{molecules}$, and m are the number of molecules, and the evaporation rate, respectively. As can be seen from this, the evaporation rate increases exponentially for each case until the droplet evaporation rate is constant. The constant evaporation rate can be attributed to the droplet evaporation reaching the Leidenfrost state and the evaporation being provided only by radiation.

The 1-D temperature distribution of the silica slab and water droplet can be observed in Figure 4.7 in which blue, green and orange lines represent energy of water, silica, and total system, respectively. In addition, the yellow and blue squares denote the silica temperature and the water temperature, respectively. The temperature of the silica substrate is ramped from 300K to 800K in 5ns. At the very beginning of the evaporation, the temperature of silica and water continues to increase almost the same and energy change in water shows an increase. In this stage, evaporation only develops at the liquid-vapor interface. The water temperature continues to increase until it reaches its saturation temperature. Then, the heat transferred to the water increases the temperature, but it is mainly used for phase-change by boiling. While sensible enthalpy increases with increase in water and vapor temperatures, latent enthalpy increases by water-to-vapor phase-change. After a certain point, the temperature difference between silica and water increases with the formation of the vapor bubbles inside the droplet. The energy change of water remains constant until some extent, but it starts to decrease with the effect of vapor formation at the solid-liquid interface. Here the locally confined vapor behaves as an insulation layer between substrate and the droplet, and it aggregates heat transfer. As the time elapses, a vapor layer occurs at interface and solid-liquid contact disappears. This phenomenon called as Leidenfrost. After the Leidenfrost point is reached, the evaporation rate starts to decrease, and it is additionally dominated by radiative heat transfer.

Therefore, while the energy change in silica remains constant, energy change in water decreases due to the radiation losses as can be seen in Figure 4.7.

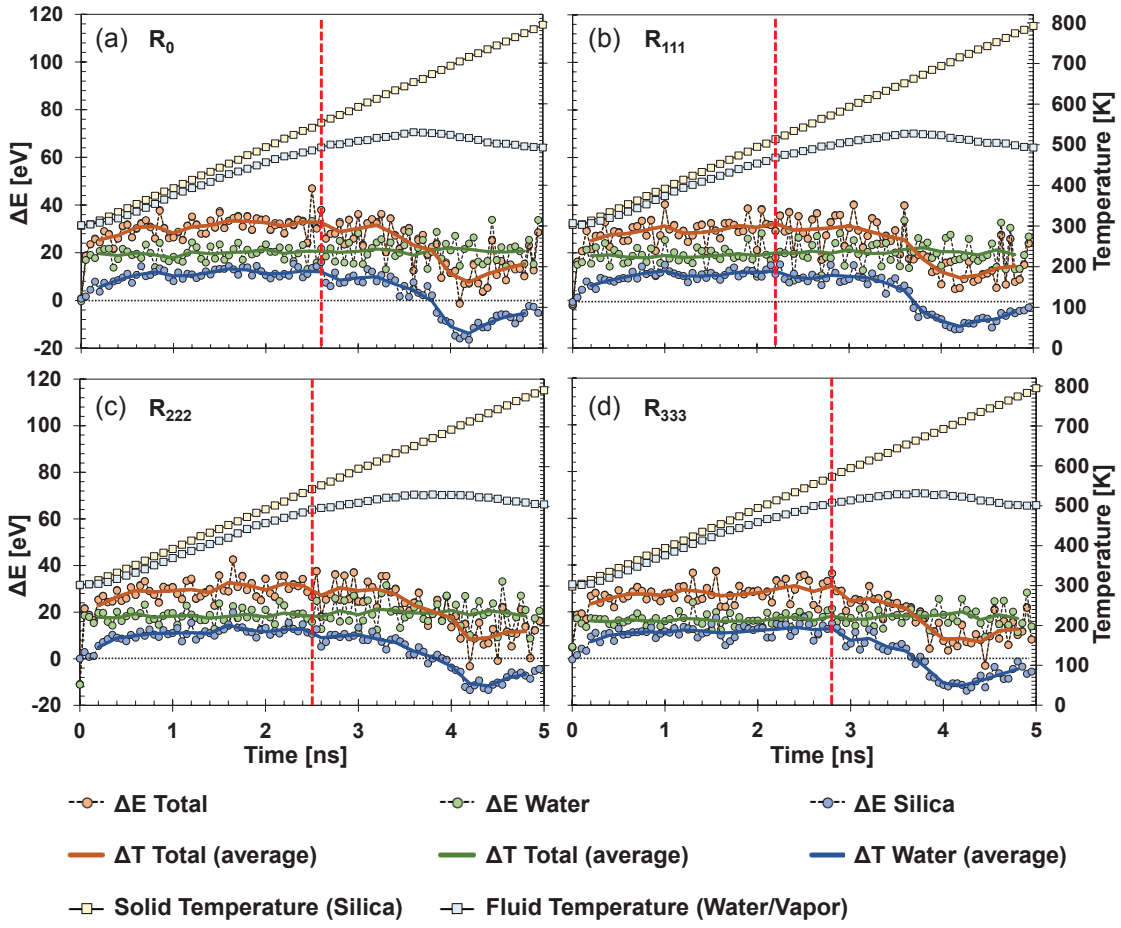

Figure 4.7. The evolution of energy change and temperature during evaporation in four different surface structure types of (a) R_0, (b) R_{111}, (c) R_{222}, and (d) R_{333}.

As described detailed in droplet evaporation and Leidenfrost phenomena part, changing surface properties, including wettability, roughness and porosity, has a tremendous influence on Leidenfrost drops. Figure 4.7 demonstrates the evolution of energy change and temperature values for four different surface roughness types. In all cases, maximum water temperature almost equals 530K. However, the times of reaching the maximum temperatures differ for each case. While R_0 case reaches the maximum temperature at 3.6 ns, R_{111} and R_{333} reach the maximum temperature at 3.7 ns and R_{222} at 3.8 ns.

The interface thermal resistance distribution of the systems is shown in Figure 4.8. The interfacial thermal resistance (R) of the system is recorded every 100 ps interval

throughout the total simulation time of 5 ns. The R of the system can be calculated by using the formulas below,

$$\frac{\partial E_t}{\partial t} = \frac{A \times (T_{Si} - T_w)}{R} \tag{4.2}$$

$$E_t = -\frac{A}{R}\int (T_{si} - T_w)dt + E_0 \tag{4.3}$$

where A is the interfacial area, E_t is system energy of the water at that time t. E_0 is initial energy of water, T_{si} and T_w are silica and water temperature at that time t. The equation 4.2 and equation 4.3 can also be related with equation 1.9. The heat flux term in equation 1.9 can be represented with energy and time interval terms which can be written as,

$$q = \frac{\partial E}{\partial t \times A} \tag{4.4}$$

Due to the constant diffusion of heat flow with time, the R of various time periods might change. R values have different characteristic which can be related with the temperature difference between silica and water ($\Delta T = T_{si} - T_w$). The temperature difference between silica and water is also plotted in Figure 4.8, represented with the colored rectangular markers with every 100ps time step. The temperature difference can be divided into four segments. In the first segment of the system, R is increasing. Then, in the second segment R can be treated constant, and can be determined by linear fitting. In the third segment R values are increasing due to the increasing temperature gap between solid liquid. In the last segment, no interfacial thermal resistance measurement can be made due to the complete evaporation of the droplet. Hence, the calculated values decrease rapidly after this point and even give negative results. For these reasons, these values are not included in Figure 4.8. On the other side, droplet temperature increases uniformly with increasing surface temperature.

R values of two cases in Figure 4.8 are represented by circular and triangle markers and the black line is the average of them. The initial slow trend increase of R in the system can be explained by the theory that the R will increase with the increase in temperature between solid and liquid, explained in research by Barisik and Beskok[102].

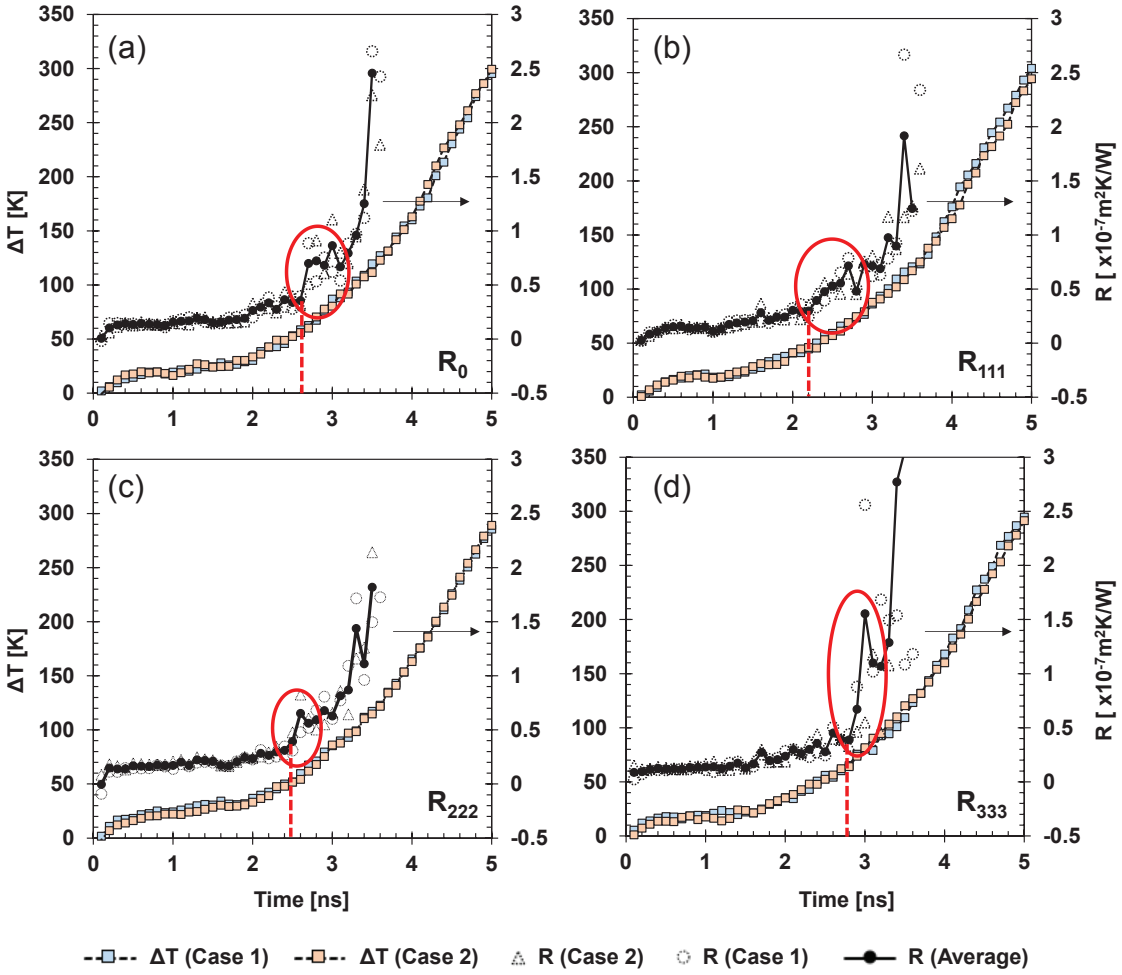

Figure 4.8. The interfacial thermal resistance (R) of silica/water, corresponds to blue and red circles. The temperatue differece between silica and water, corresponds to blue and pink squares . (a) R_0 surface, (b) R_{111} surface, (c) R_{222} surface, (d) R_{333} surface.

As mentioned previously, when evaporation rate reaches the Leidenfrost point, the solid-liquid contact disappears since a vapor layer intervenes between solid substrate and water droplet. This situation causes a dramatic increase in interfacial thermal resistance regardless of R increasing with temperature difference between solid-liquid increase. Sudden jumps in resistance values (highlighted by red ellipsis) are clearly shown in Figure 4.8 for each surface structure case. The Leidenfrost points correspond to 2.60ns, 2.20ns, 2.50ns and 2.80ns for R_0, R_{111}, R_{222} and R_{333} cases, respectively. The jumps (sudden increase) in R values are (R:0.35→0.70), (R:0.30→0.71), (R:0.31→0.65) and (R:0.38→1.55) for the cases in same respect. Evaporation process reaches the Leidenfrost point at latest in R_{333} case, but sudden jump in resistance value is the maximum.

According to these Leidenfrost points, the silica surface and water temperatures are found to be 553.96K and 492.98K for R_0, 513.99K and 468.66K for R_{111}, 543.79K and 492.1K for R_{222}, and 572.63 and 508.06 for R_{333}, respectively.

As expected, Leidenfrost point to increase with increasing surface structure. Aside from the R_0 surface, the Leidenfrost point is pushed to the higher surface temperatures with the increasing roughness. These situations show that the roughness causes a delay in droplet evaporation at reaching the Leidenfrost point.

4.3. Conclusion

In this study, MD simulations for nanosized droplet evaporation are conducted. This system was built to evaluate the behavior of the droplet on different surface structures during evaporation. To study the effect of nanopatterned surfaces on the evaporation various surface structures are designed. Each layer of honeycomb structures is removed from surface to create a surface roughness. The surfaces called as R_0, R_{111}, R_{222}, and R_{333} depending on their horizontal and vertical removal of the honeycomb structure. The water droplet evaporation has been explored during heating of the silica surface. The temperature distribution along z-direction of the droplets shows that there is a systematically temperature increase for silica surface. On the other hand, same distributions show that water temperature increase at first with the heating surface but eventually, it become almost constant. Even, it is decreases when the droplet evaporates which can be explained by volume effect of the simulation domains. It was discovered that the evaporation rate examined in this study exponentially increased at first and remained constant after reaching the Leidenfrost state.. The energy calculations are made in this research that the energy transfer rate to the water decreases after a certain point. This behavior as can be related to the increase in the latent heat enthalpy after the phase change. It can also be related to the vapor bubble formation at the solid-liquid interface. In the study, the interfacial thermal resistance during evaporation is examined as well. It is found that at the Leidenfrost point the increase of the R with the increasing temperature difference suddenly increases and after this point, the R increases exponentially until the evaporation completes. The latest Leidenfrost point is found for R_{333} surface structure type and the highest surface temperature measured at the same point. As the roughness of the surface increases, the Leidenfrost point is pushed to higher temperatures.

CHAPTER 5

SUMMARY

In the first case of the study, with MD simulations, we examined the wetting on nano-patterned silica surfaces to better understand the pinning phenomenon. We discovered that the pinning effect on nano-patterned surfaces impacts wetting behavior. The droplet volume affects the wetting angle of the nano-patterned surfaces. The wetting angle increases with increasing droplet volume due to the pinning effect. It continues to increase until it can overcome the pinning force that is affecting it. After this pinning has influenced yield, the procedure is repeated on the next heterogeneous surface. It was discovered that the pinning effects depend directly on the droplet size determined from the droplet volume ($R_{D\text{-}FS}$). When we normalized this independent droplet radius with the matching surface structure size ($R_{D\text{-}FS}/P$), we noticed a connection between the wetting behavior of different size droplets. The pinning effect reduces and becomes insignificant as droplet size increases, and the wetting angle finds its equilibrium value dependent on the roughness of the related surface. It was observed that as surface heterogeneity increased, so did the equilibrium contact angle. The equilibrium wetting angle of surfaces rises from 95° to 106°, 111°, 115°, 119°, 122°, and 125° as the surface structure increases. The size limit for pinning effects is one of the most important findings here. The minimum and maximum contact angles of each microscopic group get closer to each other as droplet size increases, decreasing the gradient of contact angle difference. As a last and crucial finding of this study, the pinning effect diminishes when the diameter of the free-standing droplet is equivalent to 24 times the size of the surface structures.

In the second case of the study, MD simulations for force-driven water flow via surface patterned silica nanochannels were used. For the proposed surface patterns, the slip behavior of water transport in silica nanochannels with a fixed channel length is evaluated. The effects of surface roughness on slip behavior are examined by changing the surface nanostructure. We demonstrated that the formation of nano-sized surface structures on the surface alters the slip behavior, and we established a relation between the surface structures and the slip length and found out that the slip length decreases with increasing surface roughness. Surface wetting dynamics can be determined by the same

solid-liquid interactions that drive velocity slip. Wetting dynamics or contact angles can therefore predict and influence velocity slip and fluid flow. As a result, we estimated the slip lengths of these surfaces using flow behavior from seven distinct surface structures and three different solid/liquid interaction parameters. Therefore, we used suggested theories to compare the slip behavior of different designed surface structures with contact angles measured on these structured surfaces. We discovered that our findings are better in line with the proposed hypothesis of Huang et al. Despite the fact that our results are similar to this proposed theory, we only found one-to-one compatibility for the flat surface. The reason for this, we believe, is that as the size of surface structure size increases, the friction increases, and the slip length reduces. It has also been found that this theory becomes less compatible as the degree of surface roughness increases.

In the third case of the study, MD simulations for nanosized droplet evaporation are performed in this work. This system was created to better understand how droplets behave on various surface structures during evaporation. Four distinct surface configurations are developed to investigate the influence of nanopatterned surfaces on evaporation. To generate surface roughness, each layer of honeycomb structures is removed from the surface. Depending on how much of the honeycomb structure is removed horizontally and vertically, the surfaces are referred to as R_0, R_{111}, R_{222}, and R_{333}. During the heating process of the droplet, the evaporation behavior was studied. The temperature distribution of the droplets in the radial direction shows a consistently increasing temperature for the silica surface. On the other side, the same distributions reveal that water temperature rises with the heating surface at first, but then falls to a near-constant level. Even after the droplet evaporates, it decreases, which may be explained by the volume effect of the simulation domains. In this study, the evaporation rate was also investigated and it was discovered that it increased until reaching the Leidenfrost point and remained constant after this point during the evaporation process. The energy change results in this study show that after a certain point, the energy transfer rate to the water drops reduces. This phenomenon can be explained by the rise in latent heat enthalpy following the phase change. It might possibly be linked to the formation of vapor at the solid-liquid interface. Further, the interfacial thermal resistance during evaporation is also investigated in the study. The increase of the R with increasing temperature difference abruptly leaps at the Leidenfrost point, and after this point, the R grows exponentially until the evaporation is complete. For the R_{333} surface structure type, the maximum Leidenfrost point is discovered and the highest surface temperature is observed

simultaneously. Aside from R_0 surface, with increased roughness, the Leidenfrost point is pushed to higher surface temperatures.

REFERENCES

(1) Gad-El-Hak, M. The Fluid Mechanics of Microdevices—the Freeman Scholar Lecture. *J. Fluids Eng. Trans. ASME* **1999**, *121* (1), 5–33. https://doi.org/10.1115/1.2822013.

(2) Vo, T. Q.; Kim, B. Transport Phenomena of Water in Molecular Fluidic Channels. *Scientific Reports*. 2016. https://doi.org/10.1038/srep33881.

(3) Nagayama, G.; Cheng, P. Effects of Interface Wettability on Microscale Flow by Molecular Dynamics Simulation. *Int. J. Heat Mass Transf.* **2004**, *47* (3), 501–513. https://doi.org/10.1016/j.ijheatmasstransfer.2003.07.013.

(4) Voronov, R. S.; Papavassiliou, D. V.; Lee, L. L. Boundary Slip and Wetting Properties of Interfaces: Correlation of the Contact Angle with the Slip Length. *J. Chem. Phys.* **2006**, *124* (20). https://doi.org/10.1063/1.2194019.

(5) Voronov, R. S.; Papavassiliou, D. V.; Lee, L. L. Slip Length and Contact Angle over Hydrophobic Surfaces. *Chem. Phys. Lett.* **2007**, *441* (4–6), 273–276. https://doi.org/10.1016/j.cplett.2007.05.013.

(6) Voronov, R. S.; Papavassiliou, D. V.; Lee, L. L. Review of Fluid Slip over Superhydrophobic Surfaces and Its Dependence on the Contact Angle. *Ind. Eng. Chem. Res.* **2008**, *47* (8), 2455–2477. https://doi.org/10.1021/ie0712941.

(7) Kim, B. H.; Beskok, A.; Cagin, T. Thermal Interactions in Nanoscale Fluid Flow: Molecular Dynamics Simulations with Solid-Liquid Interfaces. *Microfluid. Nanofluidics* **2008**, *5* (4), 551–559. https://doi.org/10.1007/s10404-008-0267-7.

(8) Ghorbanian, J.; Beskok, A. Scale Effects in Nano-Channel Liquid Flows. *Microfluid. Nanofluidics* **2016**, *20* (8). https://doi.org/10.1007/s10404-016-1790-6.

(9) Koklu, A.; Li, J.; Sengor, S.; Beskok, A. Pressure-Driven Water Flow through Hydrophilic Alumina Nanomembranes. *Microfluid. Nanofluidics* **2017**, *21* (7), 1–11. https://doi.org/10.1007/s10404-017-1960-1.

(10) Ghorbanian, J.; Celebi, A. T.; Beskok, A. A Phenomenological Continuum Model for Force-Driven Nano-Channel Liquid Flows. *Journal of Chemical Physics*. 2016. https://doi.org/10.1063/1.4967294.

(11) Ying, Y. P.; Kamarudin, S. K.; Masdar, M. S. Silica-Related Membranes in Fuel Cell Applications: An Overview. *Int. J. Hydrogen Energy* **2018**, *43* (33), 16068–16084. https://doi.org/10.1016/j.ijhydene.2018.06.171.

(12) Sun, H.; Zhao, H.; Qi, N.; Li, Y. Simulation to Enhance Shale Gas Recovery Using Carbon Dioxide in Silica Nanopores with Different Sizes. *Energy Technol.* **2017**, *5* (11), 2065–2071. https://doi.org/10.1002/ente.201700166.

(13) Vallet-Regí, M.; Colilla, M.; Izquierdo-Barba, I.; Manzano, M. Mesoporous Silica

Nanoparticles for Drug Delivery: Current Insights. *Molecules* **2018**, *23* (1), 47. https://doi.org/10.3390/molecules23010047.

(14) Neinhuis, C.; Barthlott, W. Characterization and Distribution of Water-Repellent, Self-Cleaning Plant Surfaces. *Ann. Bot.* **1997**, *79* (6), 667–677. https://doi.org/10.1006/anbo.1997.0400.

(15) Xia, Y.; Qin, D.; Yin, Y. Surface Patterning and Its Application in Wetting/Dewetting Studies. *Curr. Opin. Colloid Interface Sci.* **2001**, *6* (1), 54–64. https://doi.org/10.1016/S1359-0294(00)00088-1.

(16) Wenzel, R. N. Resistance of Solid Surfaces to Wetting by Water. *Ind. Eng. Chem.* **1936**, *28* (8), 988–994. https://doi.org/10.1021/ie50320a024.

(17) Cassie, B. D.; Cassie, A. B. D.; Baxter, S. Of Porous Surfaces,. *Trans. Faraday Soc.* **1944**, *40* (5), 546–551. https://doi.org/10.1039/tf9444000546.

(18) Guo, H. Y.; Li, Q.; Zhao, H. P.; Zhou, K.; Feng, X. Q. Functional Map of Biological and Biomimetic Materials with Hierarchical Surface Structures. *RSC Adv.* **2015**, *5* (82), 66901–66926. https://doi.org/10.1039/c5ra09490a.

(19) Feng, L.; Zhang, Y.; Xi, J.; Zhu, Y.; Wang, N.; Xia, F.; Jiang, L. Petal Effect: A Superhydrophobic State with High Adhesive Force. *Langmuir* **2008**, *24* (8), 4114–4119. https://doi.org/10.1021/la703821h.

(20) Lazo, M. A. G.; Katrantzis, I.; Vacche, S. D.; Karasu, F.; Leterrier, Y. A Facile in Situ and UV Printing Process for Bioinspired Self-Cleaning Surfaces. *Materials (Basel).* **2016**, *9* (9). https://doi.org/10.3390/ma9090738.

(21) Wang, H.; Betelu, S.; Law, B. M. Line Tension Approaching a First-Order Wetting Transition: Experimental Results from Contact Angle Measurements. *Phys. Rev. E - Stat. Nonlinear, Soft Matter Phys.* **2001**, *63* (3), 031601. https://doi.org/10.1103/physreve.63.031601.

(22) Wang, H.; Betelu, S.; Law, B. M. Line Tension Approaching a First-Order Wetting Transition: Experimental Results from Contact Angle Measurements. *Phys. Rev. E - Stat. Nonlinear, Soft Matter Phys.* **2001**, *63* (3 I), 0316011–0316011. https://doi.org/10.1103/physreve.63.031601.

(23) Ramos, S. M. M.; Charlaix, E.; Benyagoub, A. Contact Angle Hysteresis on Nano-Structured Surfaces. *Surf. Sci.* **2003**, *540* (2–3), 355–362. https://doi.org/10.1016/S0039-6028(03)00852-5.

(24) Andrews, J. E.; Wang, Y.; Sinha, S.; Chung, P. W.; Das, S. Roughness-Induced Chemical Heterogeneity Leads to Large Hydrophobicity in Wetting-Translucent Nanostructures. *J. Phys. Chem. C* **2017**, *121* (18), 10010–10017. https://doi.org/10.1021/acs.jpcc.7b02222.

(25) Huang, C.; Xu, F.; Sun, Y. Effects of Morphology, Tension and Vibration on Wettability of Graphene: A Molecular Dynamics Study. *Comput. Mater. Sci.* **2017**, *139*, 216–224. https://doi.org/10.1016/j.commatsci.2017.07.017.

(26) Zhang, H.; Chen, S.; Guo, Z.; Liu, Y.; Bresme, F.; Zhang, X. Contact Line Pinning Effects Influence Determination of the Line Tension of Droplets Adsorbed on Substrates. *J. Phys. Chem. C* **2018**, *122* (30), 17184–17189. https://doi.org/10.1021/acs.jpcc.8b03588.

(27) Wang, F. C.; Wu, H. A. Pinning and Depinning Mechanism of the Contact Line during Evaporation of Nano-Droplets Sessile on Textured Surfaces. *Soft Matter* **2013**, *9* (24), 5703–5709. https://doi.org/10.1039/c3sm50530h.

(28) Wang, F. C.; Wu, H. A. Molecular Origin of Contact Line Stick-Slip Motion during Droplet Evaporation. *Sci. Rep.* **2015**, *5*. https://doi.org/10.1038/srep17521.

(29) Forsberg, P. S. H.; Priest, C.; Brinkmann, M.; Sedev, R.; Ralston, J. Contact Line Pinning on Microstructured Surfaces for Liquids in the Wenzel State. *Langmuir* **2010**, *26* (2), 860–865. https://doi.org/10.1021/la902296d.

(30) Kim, D.; Pugno, N. M.; Ryu, S. Wetting Theory for Small Droplets on Textured Solid Surfaces. *Sci. Rep.* **2016**, *6*, 1–8. https://doi.org/10.1038/srep37813.

(31) Hong, S. Do; Ha, M. Y.; Balachandar, S. Static and Dynamic Contact Angles of Water Droplet on a Solid Surface Using Molecular Dynamics Simulation. *J. Colloid Interface Sci.* **2009**, *339* (1), 187–195. https://doi.org/10.1016/j.jcis.2009.07.048.

(32) Reyssat, M.; Quéré, D. Contact Angle Hysteresis Generated by Strong Dilute Defects. *J. Phys. Chem. B* **2009**, *113* (12), 3906–3909. https://doi.org/10.1021/jp8066876.

(33) Cao, B. Y.; Chen, M.; Guo, Z. Y. Liquid Flow in Surface-Nanostructured Channels Studied by Molecular Dynamics Simulation. *Phys. Rev. E - Stat. Nonlinear, Soft Matter Phys.* **2006**, *74* (6), 1–7. https://doi.org/10.1103/PhysRevE.74.066311.

(34) Sofos, F. D.; Karakasidis, T. E.; Liakopoulos, A. Effects of Wall Roughness on Flow in Nanochannels. *Physical Review E - Statistical, Nonlinear, and Soft Matter Physics*. 2009. https://doi.org/10.1103/PhysRevE.79.026305.

(35) Cottin-Bizonne, C.; Cross, B.; Steinberger, A.; Charlaix, E. Boundary Slip on Smooth Hydrophobic Surfaces: Intrinsic Effects and Possible Artifacts. *Phys. Rev. Lett.* **2005**, *94* (5), 1–4. https://doi.org/10.1103/PhysRevLett.94.056102.

(36) Vinogradova, O. I.; Belyaev, A. V. Wetting, Roughness and Flow Boundary Conditions. *J. Phys. Condens. Matter* **2011**, *23* (18). https://doi.org/10.1088/0953-8984/23/18/184104.

(37) Zhu, Y.; Granick, S. Limits of the Hydrodynamic No-Slip Boundary Condition. *Phys. Rev. Lett.* **2002**, *88* (10), 4. https://doi.org/10.1103/PhysRevLett.88.106102.

(38) Vinogradova, O. I.; Yakubov, G. E. Surface Roughness and Hydrodynamic Boundary Conditions. *Phys. Rev. E - Stat. Nonlinear, Soft Matter Phys.* **2006**, *73* (4), 1–4. https://doi.org/10.1103/PhysRevE.73.045302.

(39) Bonaccurso, E.; Butt, H. J.; Craig, V. S. J. Surface Roughness and Hydrodynamic

Boundary Slip of a Newtonian Fluid in a Completely Wetting System. *Phys. Rev. Lett.* **2003**, *90* (14), 4. https://doi.org/10.1103/PhysRevLett.90.144501.

(40) Joseph, P.; Tabeling, P. Direct Measurement of the Apparent Slip Length. *Phys. Rev. E - Stat. Nonlinear, Soft Matter Phys.* **2005**, *71* (3), 1–4. https://doi.org/10.1103/PhysRevE.71.035303.

(41) Huang, D. M.; Sendner, C.; Horinek, D.; Netz, R. R.; Bocquet, L. Water Slippage versus Contact Angle: A Quasiuniversal Relationship. *Physical Review Letters*. 2008. https://doi.org/10.1103/PhysRevLett.101.226101.

(42) Cho, J. H. J.; Law, B. M.; Rieutord, F. Dipole-Dependent Slip of Newtonian Liquids at Smooth Solid Hydrophobic Surfaces. *Phys. Rev. Lett.* **2004**, *92* (16), 1–4. https://doi.org/10.1103/PhysRevLett.92.166102.

(43) Richardson, S. On the No-Slip Boundary Condition. *J. Fluid Mech.* **1973**, *59* (4), 707–719.

(44) Quéré, D. Fakir Droplets. *Nat. Mater.* **2002**, *1* (1), 14–15. https://doi.org/10.1038/nmat715.

(45) Gennes, P. G. De. On Fluid/Wall Slippage. *Langmuir* **2002**, *18*, 3413–3414.

(46) Sendner, C.; Horinek, D.; Bocquet, L.; Netz, R. R. Interfacial Water at Hydrophobic and Hydrophilic Surfaces: Slip, Viscosity, and Diffusion. *Langmuir* **2009**, *25* (18), 10768–10781. https://doi.org/10.1021/la901314b.

(47) Yen, T. H.; Soong, C. Y. Effective Boundary Slip and Wetting Characteristics of Water on Substrates with Effects of Surface Morphology. *Molecular Physics*. 2016, pp 797–809. https://doi.org/10.1080/00268976.2015.1119899.

(48) Ramos-Alvarado, B.; Kumar, S.; Peterson, G. P. Hydrodynamic Slip in Silicon Nanochannels. *Physical Review E*. 2016. https://doi.org/10.1103/PhysRevE.93.033117.

(49) Sokhan, V. P.; Nicholson, D.; Quirke, N. Fluid Flow in Nanopores: An Examination of Hydrodynamic Boundary Conditions. *J. Chem. Phys.* **2001**, *115* (8), 3878–3887. https://doi.org/10.1063/1.1387976.

(50) Kalyoncu, G.; Barisik, M. Analytical Solution of Micro-/Nanoscale Convective Liquid Flows in Tubes and Slits. *Microfluidics and Nanofluidics*. 2017. https://doi.org/10.1007/s10404-017-1985-5.

(51) Yang, C.; Nakayama, A. A Synthesis of Tortuosity and Dispersion in Effective Thermal Conductivity of Porous Media. *Int. J. Heat Mass Transf.* **2010**, *53* (15–16), 3222–3230. https://doi.org/10.1016/j.ijheatmasstransfer.2010.03.004.

(52) Luo, T.; Chen, G. Nanoscale Heat Transfer-from Computation to Experiment. *Phys. Chem. Chem. Phys.* **2013**, *15* (10), 3389–3412. https://doi.org/10.1039/c2cp43771f.

(53) Kapitza, P. L. Heat Transfer and Superfluidity of Helium II. *Phys. Rev.* **1941**, *60*,

354–355. https://doi.org/10.1016/b978-0-08-019817-0.50031-8.

(54) Lim, J. A.; Lee, W. H.; Lee, H. S.; Lee, J. H.; Park, Y. D.; Cho, K. Self-Organization of Ink-Jet-Printed Triisopropylsilylethynyl Pentacene via Evaporation-Induced Flows in a Drying Droplet. *Adv. Funct. Mater.* **2008**, *18* (2), 229–234. https://doi.org/10.1002/adfm.200700859.

(55) Bigioni, T. P.; Lin, X. M.; Nguyen, T. T.; Corwin, E. I.; Witten, T. A.; Jaeger, H. M. Kinetically Driven Self Assembly of Highly Ordered Nanoparticle Monolayers. *Nat. Mater.* **2006**, *5* (4), 265–270. https://doi.org/10.1038/nmat1611.

(56) Norris, D. J.; Arlinghaus, E. G.; Meng, L.; Heiny, R.; Scriven, L. E. Opaline Photonic Crystals: How Does Self-Assembly Work? *Adv. Mater.* **2004**, *16* (16), 1393–1399. https://doi.org/10.1002/adma.200400455.

(57) Birdi, K. S.; Vu, D. T.; Winter, A. A Study of the Evaporation Rates of Small Water Drops Placed on a Solid Surface. *J. Phys. Chem.* **1989**, *93* (9), 3702–3703. https://doi.org/10.1021/j100346a065.

(58) Erbil, H. Y.; McHale, G.; Newton, M. I. Drop Evaporation on Solid Surfaces: Constant Contact Angle Mode. *Langmuir* **2002**, *18* (7), 2636–2641. https://doi.org/10.1021/la011470p.

(59) Xu, W.; Leeladhar, R.; Kang, Y. T.; Choi, C. H. Evaporation Kinetics of Sessile Water Droplets on Micropillared Superhydrophobic Surfaces. *Langmuir* **2013**, *29* (20), 6032–6041. https://doi.org/10.1021/la400452e.

(60) Rowan, S. M.; Newton, M. I.; McHale, G. Evaporation of Microdroplets and the Wetting of Solid Surfaces. *J. Phys. Chem.* **1995**, *99* (35), 13268–13271. https://doi.org/10.1021/j100035a034.

(61) Cachile, M.; Bénichou, O.; Cazabat, A. M. Evaporating Droplets of Completely Wetting Liquids. *Langmuir* **2002**, *18* (21), 7985–7990. https://doi.org/10.1021/la020231e.

(62) Hołyst, R.; Litniewski, M. Heat Transfer at the Nanoscale: Evaporation of Nanodroplets. *Phys. Rev. Lett.* **2008**, *100* (5), 3–6. https://doi.org/10.1103/PhysRevLett.100.055701.

(63) Nguyen, T. A. H.; Nguyen, A. V.; Hampton, M. A.; Xu, Z. P.; Huang, L.; Rudolph, V. Theoretical and Experimental Analysis of Droplet Evaporation on Solid Surfaces. *Chem. Eng. Sci.* **2012**, *69* (1), 522–529. https://doi.org/10.1016/j.ces.2011.11.009.

(64) Maxwell, J. C. *The Scientific Papers of James Clerk Maxwell*; Niven, W. D., Ed.; Cambridge University Press: Cambridge, 2011. https://doi.org/10.1017/CBO9780511710377.

(65) Picknett, R. G.; Bexon, R. The Evaporation of Sessile or Pendant Drops in Still Air. *J. Colloid Interface Sci.* **1977**, *61* (2), 336–350. https://doi.org/10.1016/0021-9797(77)90396-4.

(66) Bourgès-Monnier, C.; Shanahan, M. E. R. Influence of Evaporation on Contact Angle. *Langmuir* **1995**, *11* (7), 2820–2829. https://doi.org/10.1021/la00007a076.

(67) Soolaman, D. M.; Yu, H.-Z. Water Microdroplets on Molecularly Tailored Surfaces: Correlation between Wetting Hysteresis and Evaporation Mode Switching. *J. Phys. Chem. B* **2005**, *109* (38), 17967–17973. https://doi.org/10.1021/jp051182s.

(68) Leidenfrost, J. G. On the Fixation of Water in Diverse Fire. *Int. J. Heat Mass Transf.* **1966**, *9* (11), 1153–1166. https://doi.org/10.1016/0017-9310(66)90111-6.

(69) Talari, V.; Behar, P.; Lu, Y.; Haryadi, E.; Liu, D. Leidenfrost Drops on Micro/Nanostructured Surfaces. *Front. Energy* **2018**, *12* (1), 22–42. https://doi.org/10.1007/s11708-018-0541-7.

(70) Quéré, D. Wetting and Roughness. *Annu. Rev. Mater. Res.* **2008**, *38* (1), 71–99. https://doi.org/10.1146/annurev.matsci.38.060407.132434.

(71) Bernardin, J. D.; Mudawar, I. The Leidenfrost Point: Experimental Study and Assessment of Existing Models. *J. Heat Transfer* **1999**, *121* (4), 894–903. https://doi.org/10.1115/1.2826080.

(72) Kim, H.; Truong, B.; Buongiorno, J.; Hu, L. W. On the Effect of Surface Roughness Height, Wettability, and Nanoporosity on Leidenfrost Phenomena. *Appl. Phys. Lett.* **2011**, *98* (8), 2011–2014. https://doi.org/10.1063/1.3560060.

(73) Kwon, H. M.; Bird, J. C.; Varanasi, K. K. Increasing Leidenfrost Point Using Micro-Nano Hierarchical Surface Structures. *Appl. Phys. Lett.* **2013**, *103* (20). https://doi.org/10.1063/1.4828673.

(74) Arnaldo Del Cerro, D.; Marín, Á. G.; Römer, G. R. B. E.; Pathiraj, B.; Lohse, D.; Huis In 'T Veld, A. J. Leidenfrost Point Reduction on Micropatterned Metallic Surfaces. *Langmuir* **2012**, *28* (42), 15106–15110. https://doi.org/10.1021/la302181f.

(75) Tran, T.; Staat, H. J. J.; Susarrey-Arce, A.; Foertsch, T. C.; Van Houselt, A.; Gardeniers, H. J. G. E.; Prosperetti, A.; Lohse, D.; Sun, C. Droplet Impact on Superheated Micro-Structured Surfaces. *Soft Matter* **2013**, *9* (12), 3272–3282. https://doi.org/10.1039/c3sm27643k.

(76) Park, I. W.; Fernandino, M.; Dorao, C. A. Effect of Micropillar Characteristics on Leidenfrost Temperature of Impacting Droplets. July 10, 2016. https://doi.org/10.1115/ICNMM2016-7963.

(77) Lagubeau, G.; Le Merrer, M.; Clanet, C.; Quéré, D. Leidenfrost on a Ratchet. *Nat. Phys.* **2011**, *7* (5), 395–398. https://doi.org/10.1038/nphys1925.

(78) Vakarelski, I. U.; Berry, J. D.; Chan, D. Y. C.; Thoroddsen, S. T. Leidenfrost Vapor Layers Reduce Drag without the Crisis in High Viscosity Liquids. *Phys. Rev. Lett.* **2016**, *117* (11), 114503. https://doi.org/10.1103/PhysRevLett.117.114503.

(79) Alder, B. J.; Wainwright, T. E. Phase Transition for a Hard Sphere System. *The*

Journal of Chemical Physics. 1957, pp 1208–1209. https://doi.org/10.1063/1.1743957.

(80) Rahman, A. Https://Gitlab.Kwant-Project.Org/Computational_Physics_Leiden/Course_Notes/Blob/Master/Project %201/Lecture_Notes.Md. *Phys. Rev.* **1964**, *136* (2A), 405–411.

(81) Rossky, P. J. Perspective on "Correlations in the Motion of Atoms in Liquid Argon." *Theor. Chem. Acc.* **2000**, *103* (3–4), 263–264. https://doi.org/10.1007/s002149900020.

(82) Plimpton, S. Fast Parallel Algorithms for Short-Range Molecular Dynamics. *J. Comput. Phys.* **1995**, *117* (1), 1–19. https://doi.org/10.1006/jcph.1995.1039.

(83) Stillinger, F. H.; Weber, T. A. Computer Simulation of Local Order in Condensed Phases of Silicon. *Phys. Rev. B* **1985**, *31* (8), 5262–5271. https://doi.org/10.1103/PhysRevB.31.5262.

(84) Munetoh, S.; Motooka, T.; Moriguchi, K.; Shintani, A. Interatomic Potential for Si-O Systems Using Tersoff Parameterization. *Comput. Mater. Sci.* **2007**, *39* (2), 334–339. https://doi.org/10.1016/j.commatsci.2006.06.010.

(85) Jorgensen, W. L.; Chandrasekhar, J.; Madura, J. D.; Impey, R. W.; Klein, M. L. Comparison of Simple Potential Functions for Simulating Liquid Water. *J. Chem. Phys.* **1983**, *79* (2), 926–935. https://doi.org/10.1063/1.445869.

(86) Berendsen, H. J. C.; Grigera, J. R.; Straatsma, T. P. The Missing Term in Effective Pair Potentials. *J. Phys. Chem.* **1987**, *91* (24), 6269–6271. https://doi.org/10.1021/j100308a038.

(87) Sen, T.; Barisik, M. Size Dependent Surface Charge Properties of Silica Nano-Channels: Double Layer Overlap and Inlet/Outlet Effects. *Phys. Chem. Chem. Phys.* **2018**, *20* (24), 16719–16728. https://doi.org/10.1039/c8cp01906a.

(88) Esswein, E. J.; Breitenstein, M.; Snawder, J.; Kiefer, M.; Sieber, W. K. Occupational Exposures to Respirable Crystalline Silica during Hydraulic Fracturing. *J. Occup. Environ. Hyg.* **2013**, *10* (7), 347–356. https://doi.org/10.1080/15459624.2013.788352.

(89) Forati, E.; Dill, T. J.; Tao, A. R.; Sievenpiper, D. Photoemission-Based Microelectronic Devices. *Nat. Commun.* **2016**, *7* (May), 1–8. https://doi.org/10.1038/ncomms13399.

(90) Iarlori, S.; Ceresoli, D.; Bernasconi, M.; Donadio, D.; Parrinello, M. Dehydroxylation and Silanization of the Surfaces of β-Cristobalite Silica: An Ab Initio Simulation. *J. Phys. Chem. B* **2001**, *105* (33), 8007–8013. https://doi.org/10.1021/jp010800b.

(91) Plessow, P. N.; Sánchez-Carrera, R. S.; Li, L.; Rieger, M.; Sauer, S.; Schaefer, A.; Abild-Pedersen, F. Modeling the Interface of Platinum and α-Quartz(001): Implications for Sintering. *J. Phys. Chem. C* **2016**, *120* (19), 10340–10350. https://doi.org/10.1021/acs.jpcc.6b01403.

(92) Tersoff, J. New Empirical Approach for the Structure and Energy of Covalent Systems. *Phys. Rev. B* **1988**, *37* (12), 6991–7000. https://doi.org/10.1103/PhysRevB.37.6991.

(93) Miyamoto, S.; Kollman, P. A. Settle: An Analytical Version of the SHAKE and RATTLE Algorithm for Rigid Water Models. *J. Comput. Chem.* **1992**, *13* (8), 952–962. https://doi.org/10.1002/jcc.540130805.

(94) Barisik, M.; Beskok, A. Wetting Characterisation of Silicon (1,0,0) Surface. *Molecular Simulation*. 2013, pp 700–709. https://doi.org/10.1080/08927022.2012.758854.

(95) Plimpton, S. Fast Parallel Algorithms for Short-Range Molecular Dynamics for the United States Department of Energy under Contract DE.ACO4-76DPOO789. *J. Comput. Phys.* **1995**, *117*, 1–19.

(96) Azouzi, M. E. M.; Ramboz, C.; Lenain, J. F.; Caupin, F. A Coherent Picture of Water at Extreme Negative Pressure. *Nat. Phys.* **2013**, *9* (1), 38–41. https://doi.org/10.1038/nphys2475.

(97) Joswiak, M. N.; Duff, N.; Doherty, M. F.; Peters, B. Size-Dependent Surface Free Energy and Tolman-Corrected Droplet Nucleation of TIP4P/2005 Water. *Eng. Sci. Fundam. 2014 - Core Program. Area 2014 AIChE Annu. Meet.* **2014**, *2* (3), 1157.

(98) Ozcelik, H. G.; Satiroglu, E.; Barisik, M. Size Dependent Influence of Contact Line Pinning on Wetting of Nano-Textured/Patterned Silica Surfaces. *Nanoscale* **2020**, *12* (41), 21376–21391. https://doi.org/10.1039/d0nr05392a.

(99) Celebi, A. T.; Barisik, M.; Beskok, A. Electric Field Controlled Transport of Water in Graphene Nano-Channels. *J. Chem. Phys.* **2017**, *147* (16). https://doi.org/10.1063/1.4996210.

(100) Celebi, A. T.; Barisik, M.; Beskok, A. Surface Charge-Dependent Transport of Water in Graphene Nano-Channels. *Microfluid. Nanofluidics* **2018**, *22* (1). https://doi.org/10.1007/s10404-017-2027-z.

(101) Willard Gibbs, J. *ART. LII.-On the Equilibrium of Heterogeneous Substances*; 1878.

(102) Barisik, M.; Beskok, A. Temperature Dependence of Thermal Resistance at the Water/Silicon Interface. *Int. J. Therm. Sci.* **2014**, *77*, 47–54. https://doi.org/10.1016/j.ijthermalsci.2013.10.012.